2008

Evanescent Microwave Microscopy of Porcine Skin Tissue

Richard A. Kleismit
Wright State University

EVANESCENT MICROWAVE MICROSCOPY OF PORCINE SKIN TISSUE

A thesis submitted in partial fulfillment
of the requirements for the degree of
Master of Science

By

RICHARD A. KLEISMIT
B.S., Wright State University, 1998

2008
Wright State University

WRIGHT STATE UNIVERSITY
SCHOOL OF GRADUATE STUDIES

September 12, 2008

I HEREBY RECOMMEND THAT THE THESIS PREPARED UNDER MY SUPERVISION BY Richard A. Kleismit ENTITLED Evanescent Microwave Microscopy of Porcine Skin Tissue BE ACCEPTED IN PARTIAL FUFILLMENT OF THE REQUIREMENTS FOR THE DEGREE OF Master of Science .

Brent D. Foy, Ph.D.
Thesis Director

Lok C. Lew Yan Voon, Ph.D.
Department Chairman

Committee on
Final Examination

Brent D. Foy, Ph.D.

Gregory Kozlowski, Ph.D.

Paul A. Hanny, Ph.D. DABR

Joseph F. Thomas, Jr., Ph.D.
Dean, School of Graduate Studies

Abstract

Kleismit, Richard. Msc., Department of Physics, Wright State University, 2008. Evanescent Microwave Microscopy of Porcine Skin Tissue.

This thesis describes the application of a custom designed λ/4 resonant coaxial probe to measurements of the complex permittivity of *in vitro* freshly excised porcine skin tissue. The dielectric properties of the organic material within the near field of the tip of the probe frustrates the electric field and measurably changes the resonant frequency and quality factor Q of the coaxial sensor, where the change in resonant frequency and quality factor of a tuned resonance is measured as a function of tip-sample separation. The design of the probe enables better spatial resolution than previously developed probes. The following studies were performed: (1) measurement of the complex permittivity of porcine tissue over a range of frequencies revealed values consistent with published literature; (2) the change in quality factor from the probe measurements was compared to a visual microscope analysis of histological slices from the same skin location, indicating that subsurface structures such as capillary beds, ducts of exocrine sweat glands, and vein lumen ducts can be detected; and (3) measurements of the dielectric properties of a puncture wound and several burn lesions of varying severity revealed easily detectable changes, indicating that the probe has potential for evaluating and monitoring skin conditions.

In addition, a new quantitative two point relationship between the real and imaginary parts of the material's complex permittivity related to the resonant frequency and quality factor shift using the method of images is developed, presented, and used in the above described skin studies. The two-point model describing the probe tip-sample interaction is

capable of producing quantitative complex permittivity values for organic and biological materials.

Contents

List of Figures

List of Tables

Acknowledgements

I would like to thank my advisor, Dr. Brent D. Foy for his guidance and input on the research thesis development process. I also wish to thank Dr. Gregory Kozlowski and Paul A. Hanny for serving as members of my Ph.D. defense committee.

I would also like to thank the Department of Physics and the School of Graduate Studies at Wright State University for the opportunity to obtain a M.S. in Medical Physics at Wright State University.

1 Introduction

1.1 Nature of Problem

Near-field evanescent microwave microscopy has provided the opportunity for localized measurements at microwave frequencies for fundamental and practical reasons. The primary electromagnetic quantities of greatest interest are the conductivity σ, dielectric permittivity ε, and magnetic permeability μ. Evanescent microscopy is highly suited for biological applications and is capable of imaging a variety of nonuniformities in biological materials as well as quantitatively measuring tissue conductivity, permittivity, and density variations. There is also an increasing demand to promote the development of bioactive biomaterials for soft and hard tissue engineering applications. Synthetic tissue can be enzyme and chemically modified to control cell adhesion, proliferation, and matrix production. Evanescent microwave microscopy has the ability to promote characterization of these bioactive biomaterials in a nondestructive manner. The unique features pertaining to the evanescent microwave probe are its ability to measure the local characteristic information of a material and having the advantage of depth penetration. Therefore, this nondestructive method can quantify surface and subsurface properties of the biomaterials for quality, flaw, and failure detection in medical and biomedical applications.

The traditional measurements of the dielectric properties of a material provide insight into the polarization dynamics of insulators, while the complex conductivity promotes understanding of the physics related to the collective charge properties of the material.

Electromagnetic measurements have been the foundation for emerging new device technologies as well as optimizing existing devices and processes, but the applied motivation has essentially been driven by the need for characterization and quality assurance of materials. The long-established microwave microscopes perform measurements of electromagnetic quantities on scale lengths of the free space wavelength of the microwave signal. This results in weighted average measurements over large areas of the sample. Therefore, these measurements yield an overall picture of the sample properties, where any relatively small defects or inhomogeneities within the material are masked by the averaging response. The latest microwave microscopy resonant devices, utilizing a sharpened tip, have the capability of micron resolution and relatively high sensitivity. The open-ended resonator type [1, 2] contains a mixed-mode signal in the near-field, i.e., propagative and evanescent fields, which limit quantitative analysis and resolution, since the propagative field contribution to the tip-sample signal depends on features of the material. The only aperature-ended cavity resonator design [3] is Q limited due to the inductively coupled tuning loops, which directly affects sensitivity and raises the noise floor threshold. The associated theoretical model analysis produces quantitative dielectric properties of passive insulator samples with only a partial perturbed quasi-static field solution and the model is incapable of producing conductivity values for conductors even though complex conductivity is contained within the imaginary part of complex permittivity. For near-field microscopy in the microwave regime, there is little theoretical work focusing on the particular designs presented. Issues like artifacts, sensor perturbation, measured components of the microwave signals, and biological application areas have not yet received much attention. The unique attribute of the microwave evanescent field is its ability to penetrate depth-wise into a

biological sample and sense localized quantitative material changes, in-situ without this exponentially decaying field altering the sample properties. The microwave sensor utilized in this study emits a pure evanescent field from the tip and lacks a propagative wave component in the near field and does not deposit as much heat into the biological sample as the mixed mode open-ended probes. The resolution of the evanescent probe is far superior to the open-ended impedance devices, due to the focused evanescent field emanating from the sharpened tip. The calibration of the evanescent probe is straight forward and uncomplicated, compared to open-ended impedance probes and does not require any reference liquid data accuracy and temperature dependence. The evanescent measurement system tracks the change in frequency and quality factor through S_{11} port measurements and does not require added inefficient microwave devices to separate propagative and evanescent fields or detector diodes and amplifiers, which raise the noise level and reduce sensitivity, as utilized in other systems. The two-point quantitative methodology associated with this evanescent probe is extremely fast and accurate, since it relies only on the perturbed and unperturbed frequency and Q measurements of the resonance, whereas previous methods including our own used multiple measurements between the two states.

1.2 Overview of Microwave Microscopy Techniques

Near-field microscopy in the microwave bandwidth is the oldest of all near-field disciplines. The intellectual founder of the near-field microscope effort was Synge [4], who developed the principal concept in 1928. The categories are divided into five general methods, the first of which consists of a cavity resonator with evanescent coupling to the sample and is illustrated in Figure 1(a). This was suggested by Synge [4] and demonstrated

by Soohoo [5]. In this configuration, the sample is placed in close proximity to the cavity wall containing the aperture opening. This allows an aperture-sized portion of the sample to perturb the field within the cavity, changing the cavity resonant frequency and resonant Q value. The aperture is approximately 0.5 mm in diameter and results in such a minute perturbation to the cavity, that only high loss properties of the sample can be examined, such as ferromagnetic resonance. The resolution of this method is governed by the aperture diameter. A variation of this method developed by Ash and Nichols [6] used an open hemispherical resonator with a flat plate reflector containing an aperture. The sample is placed close to the aperture, but outside the resonator. The sample to aperture distance is modulated at a constant frequency, allowing phase sensitive recovery of the reflected signal to construct a quantitative image of the sample, where the resolution is determined by the aperture diameter. A non-resonant reflection/transmission technique is shown in Figure 1(b) [7-10], where the transmission line transmits a localized signal to the sample. The complex reflection or transmission coefficient is measured, and the sample properties are deduced. The resolution of this method is governed by the diameter of the center conductor in the coaxial cable and standoff height to the sample. The resonant line technique [1, 2] has proven to be the best quantitative and the most sensitive of all the near-field microwave microscopy methods and is shown in Figure 1(c). The quarter wavelength resonant line can be either planer strip [1] or coaxial [2] and the signal conductor of the resonator is tapered to a fine point that constitutes the probe. The probe tip, in close proximity to the sample, perturbs the resonator and changes in the resonant frequency, Q, and the magnitude of reflection coefficient is monitored to create corresponding sample property images. A variation of this method utilizing a quarter wavelength coaxial cavity was developed by Gao [3]. This device

configuration uses a sharpened center conductor that protrudes through a metallic coated sapphire aperture resulting in a resolution of 100 nm and Q values limited to 30,000. The experimental work from this method is accompanied by a theoretical model analysis incorporating only a partial perturbed electric field, producing quantitative microscopy of dielectrics by model fitting frequency shift and change in Q data. The frequency shift data was model fit to conductors with no reported quantitative values [3, 11]. The sharp tip cantilever device is used primarily for magnetic resonance imaging and illustrated in Figure 1(d) [12, 13]. This probe geometry can be utilized for atomic force microscopy in addition to microwave microscopy. The instrument works by measuring the electrostatic force between the conductive tip of the probe and the sample resulting in surface topography images. The superconducting quantum interference device (SQUID) microscopy [14], which is a form of RF eddy-current imaging and shown in Figure 1(e) utilizes a DC bias placed across the loop to generate circulating RF currents, which in turn produce RF magnetic fields that impinge on the sample. The sample will generate a response current, modifying the inductance of the SQUID loop. A magnetic feed back signal is required to keep the SQUID in constant flux state and tracking changes in this feedback signal allows the mapping of the electromagnetic response of the sample. This method is broadband and quantitative with a resolution of 80 μm.

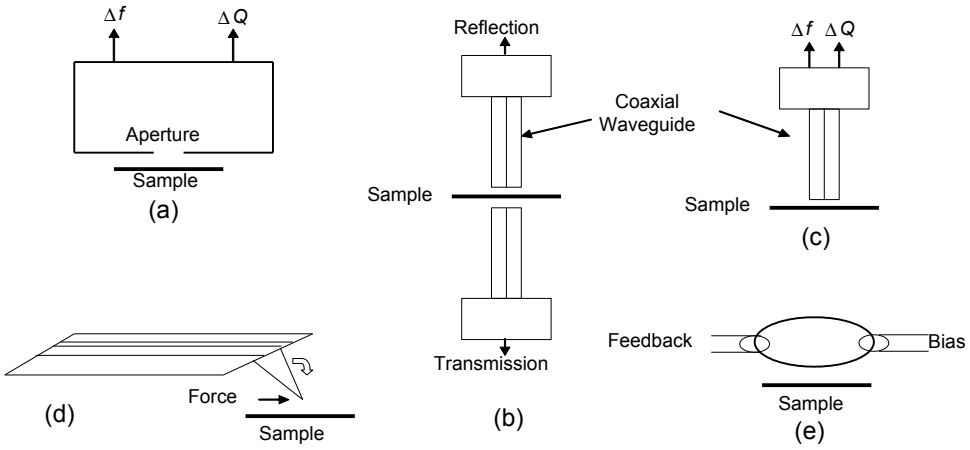

Figure 1.1: The general methods of microwave microscopy.

1.3 Overview of microwave skin tissue dielectric measurement techniques

Open-ended, coaxial, impedance/admittance probes have been traditionally used to characterize a wide range of biological materials because of their broadband capabilities and nondestructive mode of use. An open-ended coaxial transmission line forms a sensor when it is in contact with a material. The discontinuity at the open ended face of the coaxial waveguide forms an aperture plane and the electrical admittance of the probe can be measured with a vector network analyzer. It is required to develop a model that can compute the admittance from a known coaxial aperture plane geometry before an iterative algorithm can be used to 'invert' admittance measurements into complex permittivity. In measurement terms, the achievable accuracy and uncertainty of broadband, open-ended, impedance/admittance dielectric spectroscopy measurements depend on a number of factors including the probe dimensions, electrical admittance aperture plane model, calibration algorithm, precision calibration standards, frequency range and reference liquid data accuracy. The probe dimensions are selected to optimize the measurement accuracy within the frequency range and tissue of interest. The total sample volume that is actually measured

extends over the probe open surface area and is frequency dependant depth-wise into the test tissue and are of significantly large volumes. There are no previous studies utilizing this technique that have examined the dielectric properties of skin with lesions or burns, or have attempted to correlate the dielectric properties and conductivity with histological tissue structures such as blood vessels or glandular ducts.

Evanescent microwave techniques of material characterization have been used in a large number of nondestructive testing (NDT) applications [14-18], some of which could potentially be used for biological studies. In particular, evanescent microwave microscopy can be used to characterize non-uniformities in biological samples and is favorably suited for measuring conductivity, permittivity and density variations. Microwave properties are a function of complex permittivity, permeability, and free carrier concentration. In most biological tissues, moisture content, ionic species such as Na^+ and K^+, free radicals, and iron content of blood serum affect the conductivity significantly. These parameters along with density variations, which affect the dielectric constant can be mapped and quantified through evanescent microwave microscopy.

Several research groups, including our own, have used evanescent microscopy to characterize impurities and residual stress in semiconductors and superconductors, defects and non-uniformities in composite materials, and samples covering the entire conductivity range (metallic to insulating) [19-22].

1.4 Thesis Objective

The objective of this theoretical and experimental study is to utilize a near-field microwave microscopy sensor to characterize porcine skin tissue through resonant frequency

and quality factor (Q) shift measurements of an evanescent microwave probe. This thesis describes the construction and fabrication of a resonant coaxial type probe with a tapered tip extending through an end-wall aperture that is simply evanescent in the near-field. The spatial resolution of the probe is experimentally verified and an analysis of the probe sensitivity through first order estimations generated from an equivalent circuit model is presented. A model utilizing the method of images to describe the relation of frequency and Q shift of the resonator to tip-sample separation is developed. The model describing the probe tip-sample interaction is capable of producing quantitative complex permittivity values of biological tissue. An experimental investigation of the complex permittivity of porcine skin tissue in the frequency range of 1 GHz. to 15 GHz. along with skin lesions consisting of superficial puncture wound and burns are examined. The evanescent field depth and tissue subsurface structure detection was performed and verified by correlated microscopic tissue section slides.

1.4 Chapter 1 References

[1] M. Tabib-Azar, D. Akinwande, G.E. Ponchak, and S. R. LeClair, "Evanescent microwave probeson high-resistivity silicon and its application in characterization of semiconductors," Rev. Sci. Instrum., vol. 70, no.7, pp. 3083-3086, July 1999.

[2] D. E. Steinhauer, C. P. Vlahacos, S. K. Dutta, B. J. Feenstra, F. C. Wellstood, and S. M. Anlage, "Quantitative imaging of sheet resistance with a scanning near-field microwave microscope," Appl. Phys. Lett., vol. 72, no.7, pp. 861-863, Feb. 1998.

[3] C. Gao, F. Duewer, and X. D. Xiang, "Quantitative Microwave Evanescent Microscopy," Appl. Phys. Lett., vol. 75, no.19, pp. 3005-3009, 1999.

[4] E. A. Synge, " A suggested method for extending the resolution into the ultra-microscope region," Phil. Mag., vol. C 6, pp. 356-362, 1928.

[5] R. F. Soohoo, "A Microwave Magnetic Microscope," J. Appl. Phys., vol. 33, pp. 1276-1277, 1962.

[6] E. A. Ash and G.Nicholls, "Super-resolution aperture scanning microscope," Nature, vol. 237, pp. 510-512, 1972.

[7] C. A. Bryant and J. B. Gunn, "Noncontact technique for the local measurement of semiconductor resistivity," Rev. Sci. Instrum., vol. 36, pp. 1614-1617, 1965.

[8] M. A. Stuchly and S. S. Stuchly, "Coaxial line reflection methods for measuring dielectric properties of biological substances at radio and microwave frequencies- A review," IEEE Trans. Instrum. and Meas. vol. IM -29, pp. 176-183, 1980.

[9] E. C. Burdette, F. L. Cain, and J. Seals, "In vivo probe measurement technique for determining dielectric properties at VHF through microwave frequencie," IEEE Trans. Microwave Theory Tech., vol. MTT-28, pp. 414-427, April 1980.

[10] M. Fee, S. Chu, and T. W. Hansch, "Scanning electromagnetic transmission line microscope with sub-wavelength resolution," Optics Communications, vol. 69, pp. 219-224, 1989.

[11] F. Duewer, C. Gao, I. Takeuchi and X. D. Xiang, "Tip-sample distance feedback control in a scanning evanescent microwave microscope," Appl. Phys. Lett., vol. 74, no.18, pp. 2696-2698, May 1999.

[12] Z. Zhang, P. C. Hammel, and P. Wigen, Appl. Phys. Lett., "Observation of ferromagnetic resonance in a microscopic sample using magnetic resonance force microscopy," vol. 68, no. 14, pp. 2005-2007, 1996.

[13] K. Wago, D. Botkin, C. S. Yannoni, and D. Ruger, "Paramagnetic and Ferromagnetic Resonance Imaging With A Tip- On-Cantelever Magnetic Resonance Force Microscope," Appl. Phys. Lett., vol. 72, no. 21, pp. 2757-2759, May 1998.

[14] R. C. Black, F. C. Wellstood, E. Dantsker, A. H. Miklich, D. T. Nemeth, D. Koelle, and J. Clark, "Imaging radio frequency fields using a scanning SQUID microscope", Appl. Phys. Lett., vol. 66, no. 10, pp. 1267-1269, Mar. 1995.

[15] S. M. Anlage, D. E. Steinhauer, B. J. Feenstra, C. P. Vlahacos, and F. C. Wellstood, "Near-Field Microwave Microscopy of Materials Properties," in Microwave Superconductivity, ed. by H. Weinstock and M. Nisenoff, Amsterdam: Kluwer, 2001, pp. 239-269.

[16] C. Gao and X.-D. Xiang, "Quantitative microwave near-field microscopy of dielectric properties, " Review of Scientific Instruments, vol. 69, no. 11, pp. 3846-3851, Nov. 1998.

[17] X.-D. Xiang and C. Gao, "Quantitative complex electrical impedance microscopy by scanning evanescent microwave microscope," Materials Characterization, vol. 48, pp. 117-125, Apr. 2002.

[18] M. Tabib-Azar, D. Akinwande, G. Ponchak, and S.R. Leclair, "Novel physical sensors using evanescent microwave probes," Review of Scientific Instruments, vol. 70, no. 8, pp. 3381-3386, Aug. 1999.

[19] M. Tabib-Azar and S. R. LeClair, "Novel hydrogen sensors using evanescent microwave probes," Rev. Sci. Instrum., vol. 70, no.9, pp. 3707-3713, June 1999.

[20] R.A. Kleismit, G. Kozlowski, R.R. Biggers, I. Maartense, M.K. Kazimierczuk and D.B. Mast, "Characterization of local dielectric properties of superconductor $YBa_2Cu_3O_{7-\delta}$

using evanescent microwave microscopy," IEEE Trans.Appl.Supercond., vol.15, pp.2915-2918, 2005.

[21] R.A. Kleismit, M. ElAshry, G. Kozlowski, M.S. Amer, M.K. Kazimierczuk and R.R. Biggers, "Local dielectric and strain measurements in $YBa_2Cu_3O_{7-\delta}$ thin films by evanescent microscopy and Raman spectroscopy," Supercond.Sci.Technol., vol.18, pp.1197-1203, 2005.

[22] M. Tabib-Azar, P. S. Pathak, G. Ponchak, and S. Leclair, "Nondestructive super resolution imaging of defects and non-uniformities in metals, semiconductors, dielectrics, composites, and plants using evanescent microwaves," Review of Scientific Instruments, vol. 70, no. 6, pp. 2783-2792, June. 1999.

2 Evanescent Microwave Probe Characterization

2.1 Introduction

This section considers the calculation of tip-to-sample capacitance for the evanescent microwave microscopy sensor. These results are necessary if accurate equivalent circuits of resonant transmission line probes are to be constructed. The probe utilizes a sharpened center conductor with a tip radius in the micrometer range that will be modeled as a sphere. The design of the evanescent microwave probe and tuning network are discussed. An experimental study of the spatial resolution of the probe is presented along with a theoretical analysis of the sensitivity, which utilizes a lumped transmission line equivalent circuit for the resonator probe and material equivalent circuits for a conductor and insulator.

2.2 Probe Tip-Sample Capacitance

The evanescent microwave probe utilizes a chemically sharpened tip with a radius in the micrometer range and is represented as a conducting sphere, so the probe tip-to-sample coupling capacitance will be modeled as a conductive sphere over an ideal conducting plane. The capacitance of a conducting sphere over an ideal conducting plane is well characterized by Morse and Feshbach [3], and Smythe [4] and accounts for the fringing fields, which are used in this study to determine the coupling capacitance required for sensitivity analysis.

2.2.1 Capacitance of Conducting Sphere Over Perfectly Conducting Plane

The geometry of this configuration, illustrated in Figure 2.1, can be solved by two different methods. The first solution utilizes the bispherical coordinate system, which contains a mixture of Cartesian and spherical coordinates, where the field determination and capacitance calculation is through a solution of Laplace's equation.

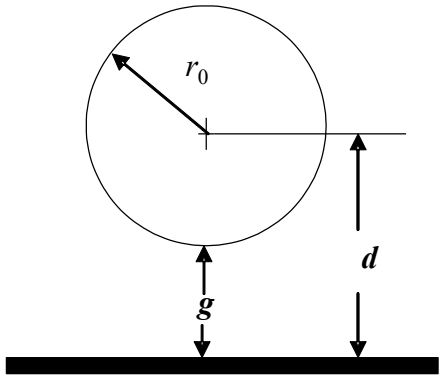

Figure 2.1: Conducting sphere above ideal conducting plane [3].

The solution of Laplace's equation in the bispherical coordinate system is a tedious problem, since it is impossible to fully separate Laplace's equation in bispherical coordinates, but it can be R-separated using the Robertson method into n ordinary differential equations and this procedure is outlined in [3] to [9]. Once Laplace's equation is R-separated the potential distribution between the conducting sphere at potential V_0 and the ideal conducting plane can be found. The determination of the total induced charge over the plane and final capacitance formulation is outlined in [3]. The capacitance between a sphere of radius r_0 and a plane at distance $g = d - r_0$ from the center of the sphere is [3]

$$C = \frac{Q}{V_0} = \sum_{p=0}^{\infty} \frac{2\sqrt{d^2 - r_0^2}}{\left[\left(d / r_0 \right) + \sqrt{\left(d / r_0 \right)^2 - 1} \right]^{2p+1} - 1}. \tag{2.1}$$

An alternate approach to forming the capacitive relation between a conducting sphere at a potential V_0 over a perfect conducting plane is through the method of images. This method is utilized by Xiang et. al. [8] for the derivation of tip-to-sample capacitance [8], [9] of an evanescent microwave microscopy probe. When a charged conducting sphere is in close proximity of a conducting plane the charge distribution on and the electric field between the conductive bodies is nonuniform. The repeated application of the method of images can be utilized to solve this problem. The formulation of the capacitance from this method results in a transcendental equation in terms of hyperbolic functions. The capacitance between a sphere of radius r_0 and a plane at distance $d = g + r_0$ from the center of the sphere is shown as

$$C = 4\pi\varepsilon_0 r_0 \sinh\alpha \sum_{n=1}^{\infty} \operatorname{csch} n\alpha, \tag{2.2}$$

where

$\alpha = \cosh^{-1}(d / r_0)$.

2.3 Evanescent Microwave Probe Description

The resonator probe is based on an open-circuit transmission line and is constructed from 0.085″ semi-rigid, copper, coaxial transmission line indicated in Figure 2.2. This type of resonator behaves as a parallel-resonant circuit when the length is a multiple of λ/2 and a series-resonant circuit for odd multiples of λ/4. In constructing the probe, the center conductor was removed along with the Teflon insulator. A sharpened tip was mounted on the center conductor and electroplated with approximately 1 micrometer of silver. The transmission-line resonator was then reconstructed by casting the sharpened, plated, center conductor inside the outer shield with high-grade paraffin. A copper end-wall aperture is

placed at the sharpened end of the coax. The aperture is sized for cutoff at the resonant frequencies desired. The sharpened point of the center conductor extends beyond the end wall aperture of the resonator by approximately twenty micrometer or less in order to maintain spatial resolution.

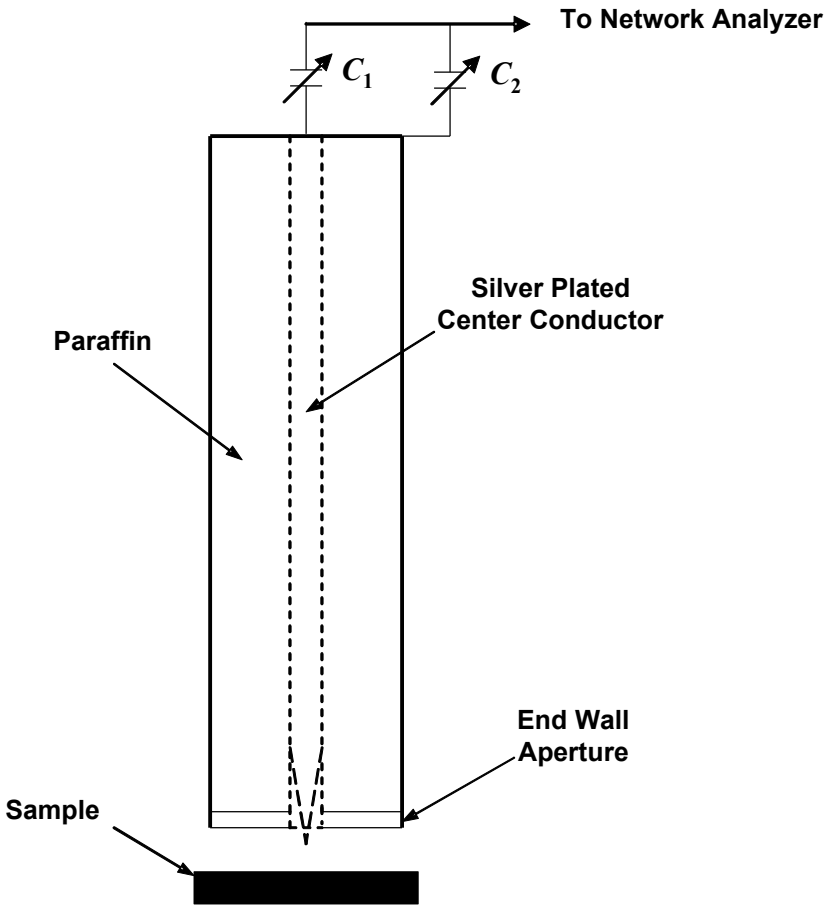

Figure 2.2: Evanescent microwave probe description [10].

The highly conductive silver-plating along with the low loss tangent of paraffin will increase the quality factor to nearly twice that of the standard Teflon filled coaxial transmission line. It is necessary to keep Q as high as possible to obtain high sensitivity. The probing field emanates from the tip, so as the tip radius decreases, the spatial resolution increases due to localization of the interaction between the tip and sample. The standing wave in the resonator

is mode converted to evanescent at the reflecting face of the end-wall aperture. The evanescent field starts decaying exponentially at this point, but the evanescent field intensity at the tip is of sufficient amplitude to penetrate a material such as a dielectric.

The resonant frequency of the probe is fine tuned by an external capacitive tuning assembly consisting of two variable 2.5-8 pF sapphire capacitors. The sapphire capacitors were chosen due to the frequency invariance of sapphire up to approximately 10 GHz. The tuning network illustrated in Figure 2.2 has one capacitor connected in line with the center conductor and the other connected from center conductor to ground allowing greater tuning versatility. The capacitive matching network will allow extremely high Q values to be obtained during experimentation, which is due to the equivalent series resistance (ESR) of the sa

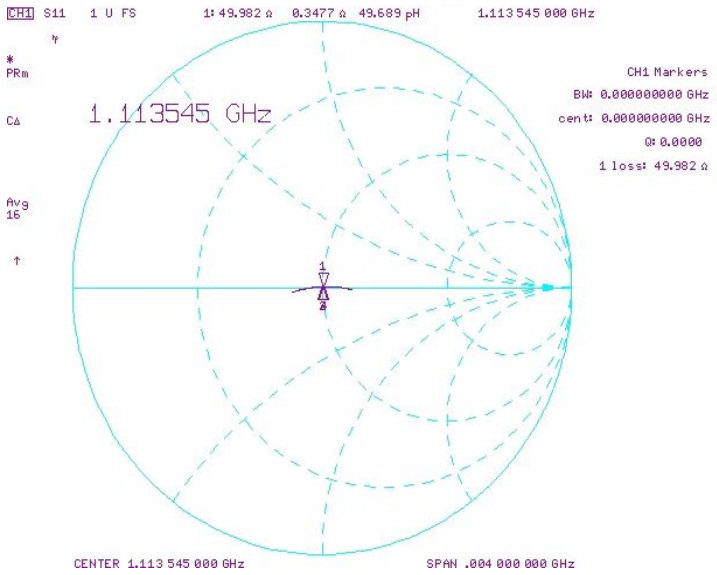

Figure 2.3: Impedance match between probe assembly and feed line.

A Smith chart plot is illustrated in Figure 2.3, of the normalized impedance match between the probe and tuning network to the 50 Ω transmission feed line at a Q of 90,000 and a frequency of 1.113545 GHz, where the impedance mismatch from the 50 Ω line is 0.018 Ω. Figure 2.4 indicates a Smith chart plot of the normalized impedance match to a 50 Ω calibration load replacing the resonant probe and tuning network to the feed line, resulting in an impedance mismatch from the 50 Ω line of 0.016 Ω. An analysis for the calculation of Q values related to the series (endwall) and shunt capacitance termination of a transverse elect

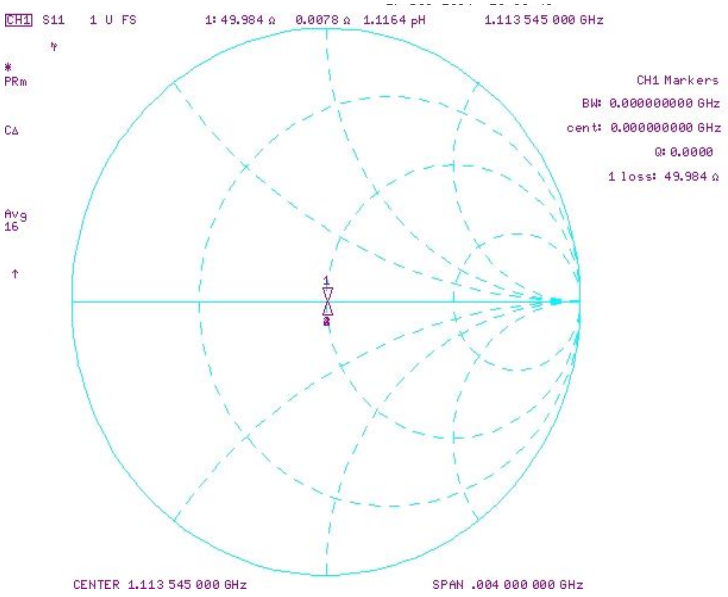

Figure 2.4: Impedance match between feed line and 50 Ω termination.

2.4 Spatial Resolution of Evanescent Microwave Probe

The resolution of the probe was experimentally verified using a sapphire polycrystalline substrate with titanium-gold etched lines from 10 μm to 1μm in width and is illustrated in

Figure 2.5. The titanium was used to allow adhesion of the gold to the substrate and is approximately 100 nm thick, while the deposition thickness of the gold is approximately 1 μm. The resonant frequency of the probe was tuned to 2.67 GHz for this experiment. The etched lines of the sample were scanned with the probe resulting in a change in frequency, Q, and magnitude of reflection coefficient plots.

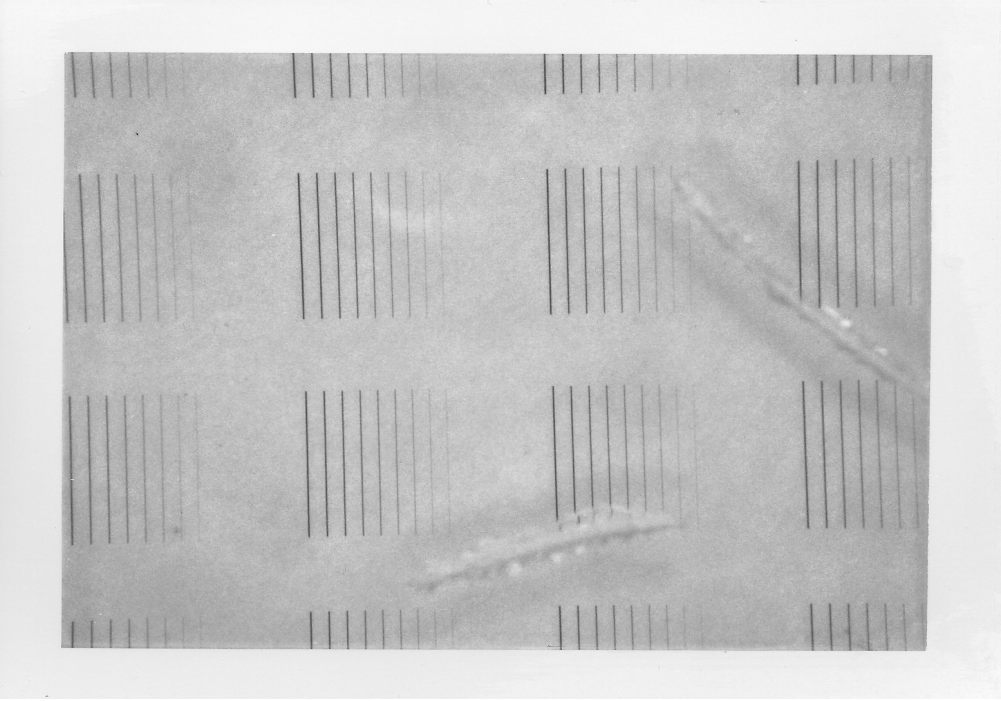

Figure 2.5: Resolution slide with Ti, Au etched lines from 1 μm to 10 μm in width [13].

It has been shown [14] that the smallest physically resolvable feature for an evanescent probe is basically governed by the characteristic size of the tip radius, along with the height at which the tip is above the desired feature. In other words to resolve a 5 μm physical feature the probe tip radius has to be less than or equal to 5 μm and should be no more than 5μm above it. Figures 2.6 to 2.8 are plots of frequency shift, change in Q, and change in reflection coefficient magnitude respectively, of an 18 μm x 20 μm scan of the 1μm wide etched line.

The measured tip radius of the probe used is 1.2 µm at a stand off height of approximately 1 µm with a 1µm data acquisition step. The area of the etched line is indicated on each plot by arrows with corresponding measurements in micrometers.

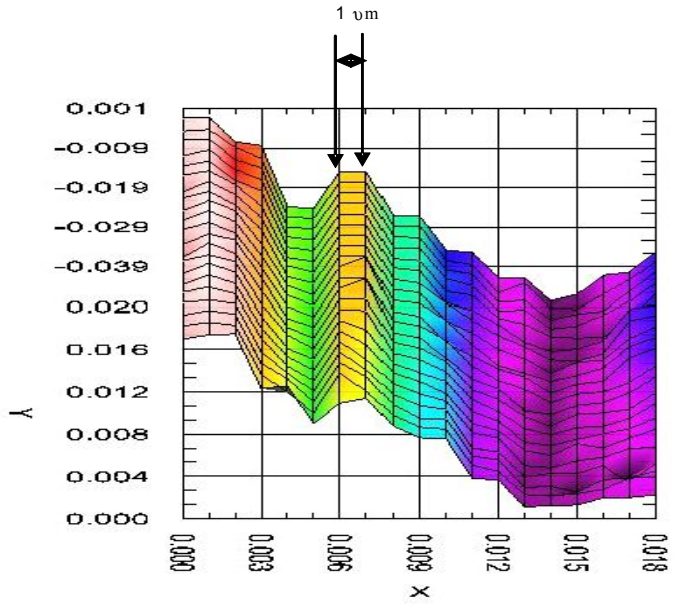

Figure 2.6: Frequency shift plot of 1 micron wide line [13].

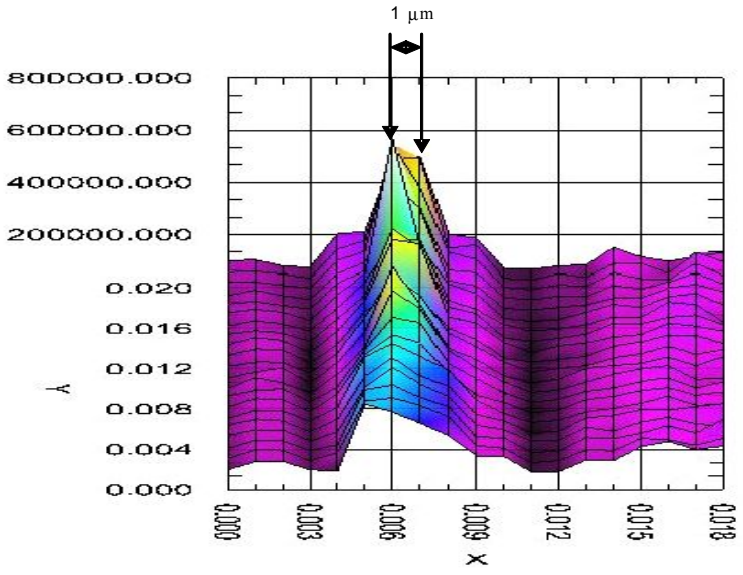

Figure 2.7: Change in Q plot of 1 micron wide line [13].

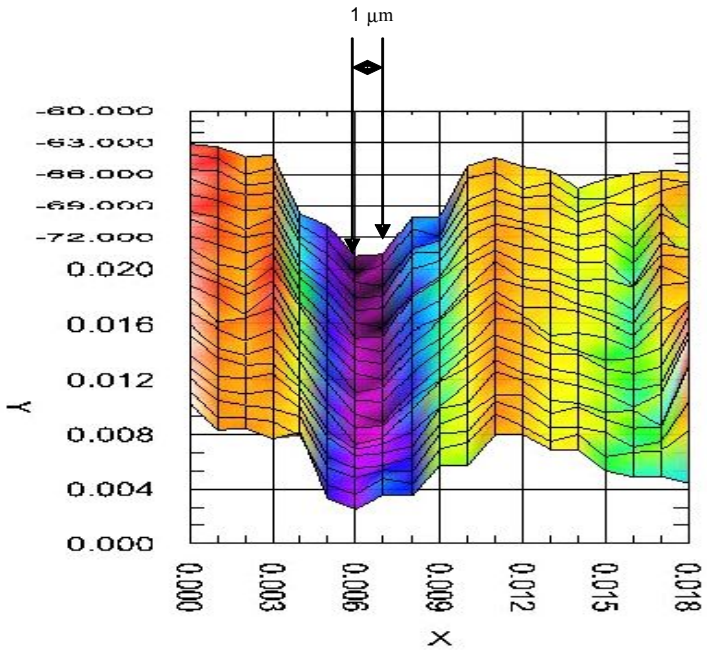

Figure 2.8: Change in reflection coefficient of 1 micron wide line [13].

The 1-micrometer width line plots indicate that even though the probe tip radius is slightly larger than 1 micrometer it is still has the ability to distinguish a 1 micron feature, which is probably due to the extremely high Q value of the tuned resonant probe. The ability of this particular evanescent microwave probe to discriminate physical features to a 1 μm level, results in the topographical resolution to be experimentally verified to 1μm.

2.5 Evanescent Microwave Probe Sensitivity Analysis

2.5.1 Introduction

The sensitivity of the evanescent microwave probe can be separated into two categories [14]. The first of which is inherent to the resonator S_r and directly proportional to the quiescent operating value Q of the resonator. The other is external to the resonator S_f and solely determined by the tip-sample interaction. The sensitivity analysis of the evanescent

microwave probe is considered separately for conductors and dielectrics utilizing a lumped transmission line equivalent circuits for the resonator probe and material equivalent circuits for the conductor and insulator.

2.5.2 Evanescent Microwave Probe Resonator Sensitivity S_r

The sensitivity approximation internal to the resonator S_r can be determined theoretically and experimentally. The theoretical value is analytically approximated by considering the lumped equivalent circuit of the resonator illustrated in Figure 2.9, which has an inherent resonant frequency ω_0 and Q associated to the lumped parameters R_0, L_0, and C_0. This configuration and associated parameters can be viewed as if the probe tip is beyond the decay length of the evanescent field from a material, or in free space.

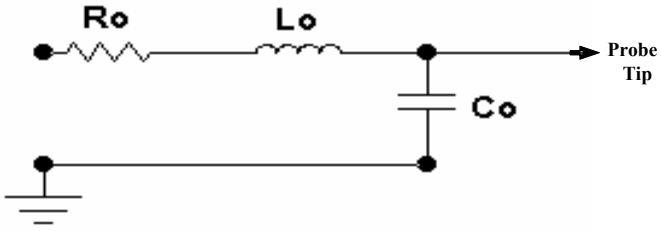

Figure 2.9: Lumped circuit model of resonator probe [13].

If the probe tip is brought into close proximity and electrically couples to the sample, the resonant frequency and Q is perturbed to a new value ω_0' and Q′ respectively and are associated to new perturbed parameters R_0', L_0', and C_0'. The total impedance looking into the terminals of the perturbed resonator coupled to a sample can be written as

$$Z_{total} = R_0'\left[1 + jQ'\left(\frac{\omega}{\omega_0'} - \frac{\omega_0'}{\omega}\right)\right]. \tag{2.3}$$

The magnitude of the reflection coefficient S_{11} is related to Z_{total} by

$$S_{11} = \frac{Z_{total} - Z_0}{Z_{total} + Z_0}, \tag{2.4}$$

where Z_0 is the characteristic impedance. If we assume critical coupling, where the resonator is matched to the characteristic impedance of the feed transmission line at resonant frequency, then $R_0' \approx Z_0$ at $\omega \approx \omega_0$ and S_r is defined as [15]

$$S_r = \frac{dS_{11}}{d\omega} \approx \frac{Q'}{\omega_0'}\left(1 - \frac{\Delta\omega}{\omega_0'}\right) \tag{2.5}$$

where $\Delta\omega = \omega - \omega_0'$.

A dielectric sample was tested using the evanescent measurement system. The unperturbed reference frequency f_0 was set at 1.216616087 GHz with a Q value of 71423 and is illustrated in the network analyzer screen capture of Figure 2.10.

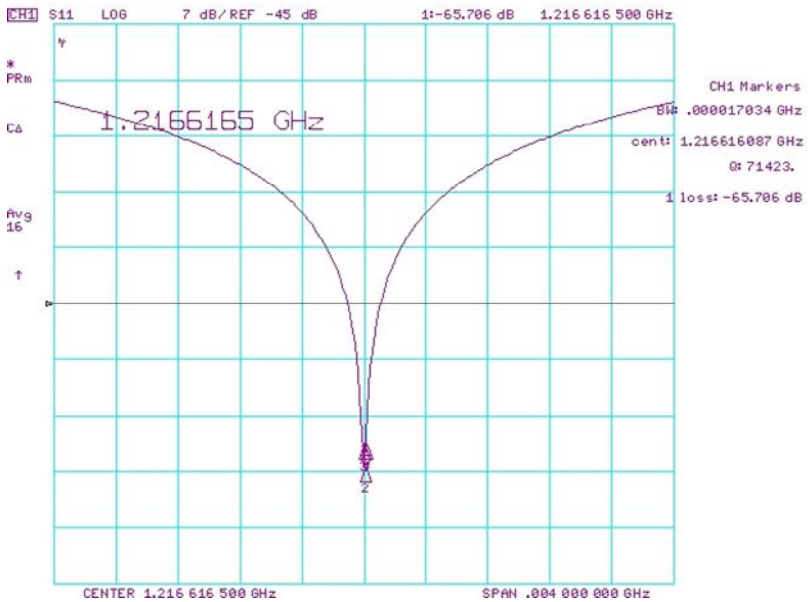

Figure 2.10: Reference resonance for sapphire dielectric sensitivity measurement.

A sapphire sample were inserted under the probe and the tip-sample distance was adjusted to 1 um, with the perturbed results indicated in Figures 2.11

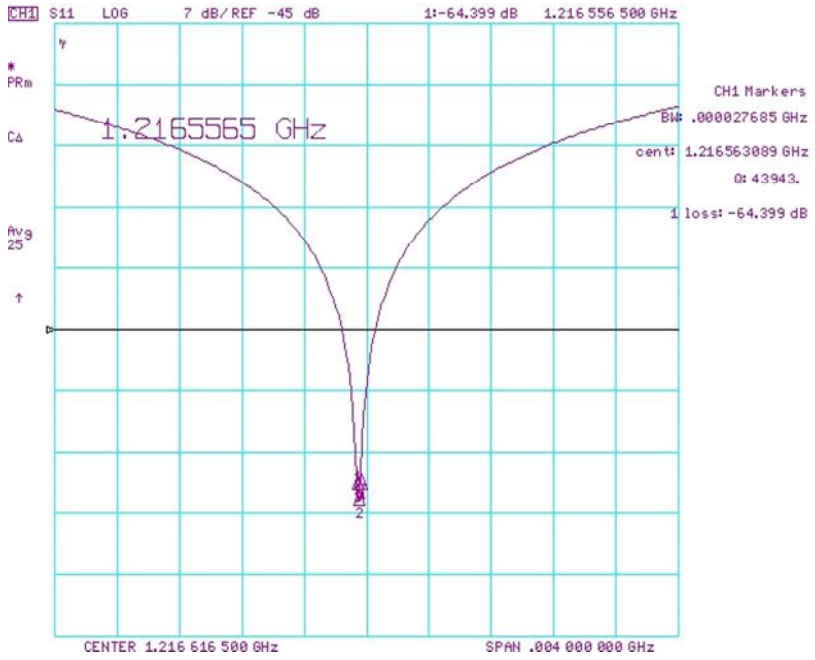

Figure 2.11: Perturbed resonance for sapphire dielectric sensitivity measurement.

The unperturbed and perturbed parameters are

$\Delta\omega$ = 332996 rad/sec, Q′ = 43943 and $\omega = 7.64389\times10^{9}$ rad/sec

$\omega_0 = 7.64422\times10^{9}$ rad/sec, Q = 71423

and utilizing these values in (2.5) results in $S_r = 5.74\times10^{-6}$. Data was collected for a copper conductor sample and the unperturbed and perturbed parameters used in Equation (2.5) are

$\Delta\omega$ = 539725 rad/sec, Q′ = 42747 and $\omega = 7.64389\times10^{9}$ rad/sec

$\omega_0 = 7.64421\times10^{9}$ rad/sec, Q = 78345, which results in $S_r = 5.59\times10^{-6}$.

2.5.3 Noise Threshold

The minimum detectable signal in an evanescent microwave microscopy system has to be greater than the noise threshold created by the resonator probe, tuning network, and coupling to the sample. The noise is generated by a resistance at an absolute temperature of T by the random motion of electrons proportional to the temperature T within the resistor. This generates random voltage fluctuations at the resistor terminal, which has zero average value, but a nonzero rms value given by Planck's black body radiation law and can be calculated by the Rayleigh-Jeans approximation [16] shown as

$$V_{n(rms)} = \sqrt{4kTBR}\,, \tag{2.6}$$

where

k = Boltzmann's constant, T = temperature in K,

B = bandwidth of the system in Hz, R = resistance in Ω.

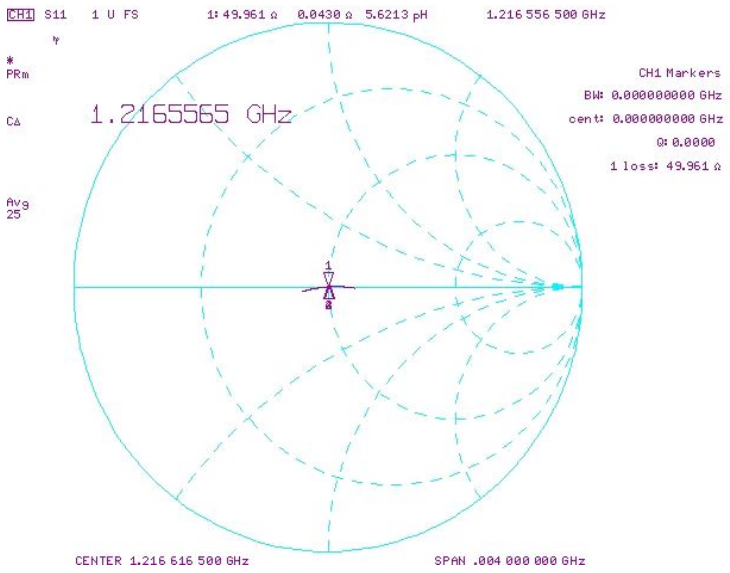

Figure 2.12: Smith chart plot corresponding to Figure 2.11.

Figure 2.12 illustrates the Smith chart plot corresponding to frequency shifted resonance of Figure 2.11, where the Q of the resonator has degraded due to the loading of the sapphire sample. The impedance mismatch from the 50 Ω line is 0.039 Ω, corresponding to a noise voltage of 0.051×10^{-6} $V_{n(rms)}$.

2.5.4 Evanescent Microwave Probe Sensitivity S_f for Conductors

The equivalent circuit model for the probe coupled to a conductor is illustrated in Figure 2.13.

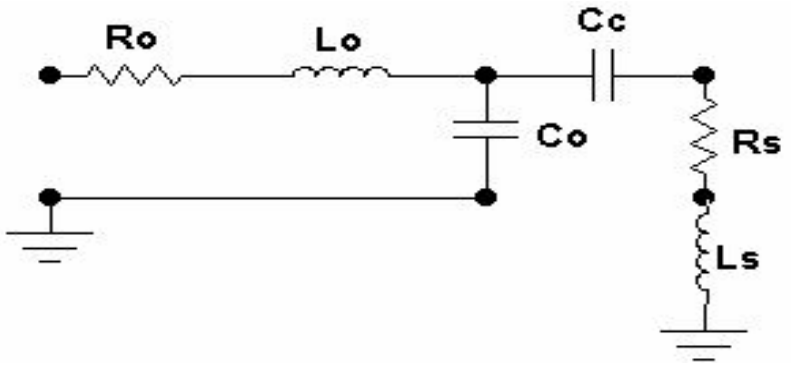

Figure 2.13: Lumped circuit of microwave probe coupled to conductor [13].

The probe is coupled to the metallic sample through the coupling capacitance C_c and the conductor is represented as the series combination of R_s and L_s. The impedance Z_1 is the series combination of C_c , R_s , and L_s and is represented as

$$Z_1 = \frac{1}{j\omega C_c} + j\omega L_s + R_s = \frac{1 + j\omega C_c R_s - \omega^2 L_s C_c}{j\omega C_c} \tag{2.7}$$

The parallel combination of Z_1 and C_0 results in

$$\frac{1}{Z_2} = j\omega C_0 + \frac{j\omega C_c}{(1-\omega^2 L_s C_c) + j\omega C_c R_s} = \frac{j\omega\left[C_c + C_0(1-\omega^2 L_s C_c) - \omega^2 C_0 C_c R_s\right]}{(1-\omega^2 L_s C_c) + j\omega C_c R_s},$$

and the impedance Z_2 is

$$Z_2 = \frac{\left(1-\omega^2 L_s C_c\right)+ j\omega C_c R_s}{j\omega[C_c + C_0\left(1-\omega^2 L_s C_c\right)-\omega^2 C_0 C_c R_s]} = -\frac{j}{\omega} Z_2' \tag{2.8}$$

The total impedance Z_{total} looking into the terminals of the probe coupled to a conductor sample is

$$Z_{total} = R_0 + j\omega L_0 - \frac{j}{\omega} Z_2' . \tag{2.9}$$

The complex impedance Z_2 can be represented as

$$Z_2 = \frac{1}{j\omega}[\mathrm{Re}(Z_2')] = -\frac{j}{\omega} Z_2' . \tag{2.10}$$

At resonance the inductive and capacitive reactance cancel therefore,

$$j\omega L_0 - \frac{j}{\omega}[\mathrm{Re}(Z_2')] = 0$$

$$\omega^2 L_0 = \mathrm{Re}(Z_2') \tag{2.11}$$

This allows us to solve for perturbed frequency ω in terms of the perturbed lumped circuit parameters in an iterative process, where we will be taking a first order approximation. The impedance Z_2' is represented as

$$Z_2' = \frac{(1-\omega^2 L_s C_c) + j\omega C_c R_s}{[C_c + C_0(1-\omega^2 L_s C_c) + j\omega C_0 C_c R]_s} \tag{2.12}$$

Taking the real part of (2.12), we have

$$\mathrm{Re}(Z_2') = \frac{C_c(1-\omega^2 L_s C_c) + C_0(1-\omega^2 L_s C_c)^2 + \omega^2 C_0 C_c^2 R_s^2}{[C_c + C_0(1-\omega^2 L_s C_c)]^2 + \omega^2 C_0^2 C_c^2 R_s^2} \tag{2.13}$$

The numerator and denominator of (2.13) are expanded, neglecting the ω^4 terms due to insignificance and factoring out $(C_c + C_0)$, then substituting back into (2.11) results in

$$\omega^2 L_0 = \frac{1}{(C_c + C_0)} \frac{1 - \omega^2 \frac{[L_s C_c (C_c + 2C_0) - C_0 C_c^2 R_s^2]}{(C_c + C_0)}}{1 - 2\omega^2 \frac{L_s C_c C_0}{(C_c + C_0)} + \omega^2 \frac{C_0^2 C_c^2 R_s^2}{(C_c + C_0)^2}} \tag{2.14}$$

The numerator and denominator of (2.14) are multiplied by

$1 - \omega^2 \frac{[L_s C_c (C_c + 2C_0) - C_0 C_c^2 R_s^2]}{(C_c + C_0)}$ resulting in

$$\omega^2 L_0 = \frac{1}{(C_c + C_0)} \frac{1}{1 + \omega^2 \frac{L_s C_c^2}{(C_c + C_0)} + \omega^2 \frac{C_0^2 C_c^2 R_s^2}{(C_c + C_0)} \left(\frac{C_0}{C_c + C_0} - 1 \right)} \tag{2.15}$$

The relation $\frac{\omega_0^2}{1 + C_c / C_0}$ with $\omega_0^2 = 1/L_0 C_0$ is substituted into (2.15) and taking the square root of both sides produces

$$\omega_0' = \omega_0 \frac{1}{\sqrt{1 + C_c / C_0}} \frac{1}{\sqrt{1 + \frac{L_s}{L_0} \left(\frac{C_c}{C_0 + C_c} \right)^2 - \frac{R_s^2 C_0}{L_0} \left(\frac{C_c}{C_0 + C_c} \right)^3}} \tag{2.16}$$

Equation (2.16) is the first order approximation for the perturbed frequency due to the coupling of the probe to a conductor. The highest order term in the denominator has an insignificant contribution and is neglected; therefore, (2.16) results in

$$\omega_0' = \omega_0 \left(\frac{1}{\sqrt{1 + C_c / C_0}} \right) \frac{1}{\sqrt{1 + \frac{L_s}{L_0} \left(\frac{C_c}{C_0 + C_c} \right)^2}} \tag{2.17}$$

The Taylor expansion of (2.17) gives

$$\omega_0' = \omega_0 \left(1 - \frac{1}{2} \frac{C_c}{C_0} \right) \left(1 - \frac{1}{2} \frac{L_s}{L_0} \frac{C_c^2}{(C_0 + C_c)^2} \right) \tag{2.18}$$

The sensitivity S_f for a conductor is defined to be [15]

$S_f = \frac{g_s R_s^2}{2\pi}\left|\frac{d\omega_0'}{dL_s}\right|$, where $g_s = \frac{A_{eff}}{\delta}$, A_{eff} is effective tip area and δ is the skin depth, therefore the sensitivity S_f for a conductor is found by taking the derivative of ω_0' with respect to L_s in (2.18) and results in

$$S_f = \frac{g_s R_s^2}{2\pi}\omega_0\left(1-\frac{C_c}{2C_0}\right)\left[\frac{1}{2L_0}\frac{C_c^2}{(C_0+C_c)^2}\right]. \tag{2.19}$$

A study of sensitivity for elemental conductors Pb and Cr was performed utilizing Equation (2.19). The associated parameters and sensitivities are tabulated in Table 2.2. The effective tip area A_{eff} was calculated using the measured tip radius r_0=3.5 μm for the Pb and Cr specimens discussed in Section 3.4.2. The ability of the probe to differentiate between regions of different conductivity Δσ/σ is defined as [15]

$$\frac{\Delta\sigma}{\sigma} = \frac{\frac{V_{n(rms)}}{V_{in}}}{S_f S_r \sigma} \tag{2.20}$$

The values of Δσ/σ for the conductors is listed in Table 2.1 and the parameters used to generate S_r and $V_{n(rms)}$ were also taken from the experimental data in Section 3.4.2 and V_{in} is the input voltage to the probe.

TABLE 2.1: Sensitivity and Associated Parameters for Conductors.

	σ (10^6 S/m)	δ (10^{-7} Ω/m)	R_s (10^{-2} Ω)	S_r (10^{-6})	S_f (10^{-2})	Δσ/σ (10^{-3})
Pb	**4.872**	**2.053**	**3.00**	**6.17**	**9.83**	**1.55**
Cr	**5.104**	**1.959**	**2.93**	**6.08**	**4.52**	**3.07**

2.5.5 Evanescent Microwave Probe Sensitivity S_f for Dielectrics

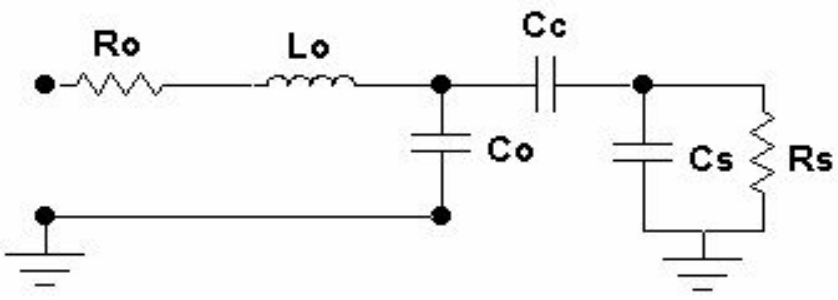

Figure 2.14: Lumped circuit of microwave probe coupled to dielectric [13].

The equivalent circuit model for the probe coupled to a dielectric is illustrated in Figure 2.14, with the probe coupled to the insulator sample through the coupling capacitance C_c and the dielectric represented as the parallel combination of R_s and C_s. The impedance Z_1 is the parallel combination of R_s and C_s and is represented as

$$Z_1 = \frac{R_s}{j\omega C_s R_s + 1} \tag{2.21}$$

The series combination of Z_1 and C_c result in

$$Z_2 = \frac{1 + j\omega C_s R_s + j\omega C_c R_s}{j\omega C_c (j\omega C_c R_s + 1)} \tag{2.22}$$

The impedance Z_3 is the parallel combination of Z_2 and C_0 and is represented as

$$Z_3 = \frac{1 + j\omega C_c R_s + j\omega C_s R}{j\omega C_c (1 + j\omega C_c R_s) + j\omega C_0 (1 + j\omega C_c R_s + j\omega C_s R_s)} = -\frac{j}{\omega} Z_3' \ . \tag{2.23}$$

The total impedance Z_{total} looking into the terminals of the probe coupled to a dielectric sample is $Z_{total} = R_0 + j\omega L_0 - \frac{j}{\omega} Z_3'$ (2.24)

The complex impedance Z_3 can be represented as

$$Z_3 = \frac{1}{j\omega}[\mathrm{Re}(Z_3')] = -\frac{j}{\omega}[\mathrm{Re}(Z_3')]. \tag{2.25}$$

At resonance the inductive and capacitive reactance cancel; therefore,

$$j\omega L_0 - \frac{j}{\omega}[\mathrm{Re}(Z_3')] = 0$$

$$\omega^2 L_0 = \mathrm{Re}(Z_3'). \tag{2.26}$$

The quantity $j\omega R_s$ is factored out in the numerator and denominator of (2.23) and the result placed into (2.26), we have

$$\omega^2 L_0 = \frac{(C_c + C_0) + \omega^2 R_s^2 (C_c + C_s)[C_c C_s + C_0 (C_c + C_s)]}{(C_c + C_0)^2 + \omega^2 R_s^2 (C_c C_s + C_0 (C_c + C_s))^2},$$

R_s is removed since it is large, so

$$\approx \frac{(C_c + C_s)}{C_c C_s + C_0 (C_c + C_s)} = \frac{1}{C_0} \frac{1}{\left[1 + \frac{C_c C_s}{C_0 (C_c + C_s)}\right]},$$

therefore

$$\omega_0'^2 = \frac{1}{L_0 C_0} \frac{1}{\left(1 + \frac{C_c C_s}{C_0 (C_c + C_s)}\right)}. \tag{2.27}$$

Solving for ω_0' in (2.27) results in

$$\omega_0' = \omega_0 \frac{1}{\sqrt{1 + \frac{C_c C_s}{C_0 (C_c + C_s)}}} \tag{2.28}$$

The first-order Taylor expansion of (2.28) gives

$$\omega_0' = \omega_0 \left(1 - \frac{1}{2} \frac{C_c C_s}{C_0 (C_c + C_s)}\right). \tag{2.29}$$

The sensitivity S_f for a dielectric is defined to be [15] $S_f = \frac{g_s}{2\pi}\left|\frac{d\omega_0'}{dC_s}\right|$, where $g_s = \frac{A_{eff}}{\xi_s}$,

A_{eff} is effective tip area and ζ_s =100 μm is evanescent wave decay length; therefore, the sensitivity S_f for a dielectric is $S_f = \frac{g_s\omega_0}{4\pi}\frac{C_c^2}{C_0(C_c+C_s)^2}$. (2.30)

A study of the sensitivity for single crystal dielectrics, MgO, YSZ, and $SrTiO_3$ was performed utilizing Equation (2.30). The associated parameters and sensitivities are tabulated in Table 2.3. The effective tip area A_{eff} was calculated using the measured tip radius r_0 = 3.5μm for the MgO, YSZ, and $SrTiO_3$ specimens discussed in Section 3.5.2. The ability of the to differentiate between regions of different permittivity Δε/ε is defined as [15]

$$\frac{\Delta\varepsilon}{\varepsilon} = \frac{\frac{V_{n(rms)}}{V_{in}}}{S_f S_r \varepsilon} \quad . \tag{2.31}$$

The values of Δε/ε for the dielectrics is listed in Table 2.2 and the parameters used to generate S_r and $V_{n(rms)}$ were also taken from the experimental data in Section 3.5.2.

TABLE 2.2: Sensitivity and Associated Parameters for Dielectrics.

	$\varepsilon'/\varepsilon_0$	$\varepsilon''/\varepsilon_0$	S_f	S_r (10^{-6})	$\Delta\varepsilon/\varepsilon$
MgO	**10**	**2×10^{-5}**	**7.12×10^{-5}**	**5.97**	**7.5×10^{-4}**
YSZ	**30**	**2×10^{-3}**	**2.93×10^{-6}**	**5.08**	**2.23×10^{-3}**
$SrTiO_3$	**300**	**0.1**	**2.97×10^{-8}**	**4.73**	**3.49×10^{-3}**

2.6 Chapter 2 References

[1] D. K. Cheng, Field and Wave Electromagnetics. 2nd Ed., New York, N.Y.: Addison-Wesley, 1992.

[2] H. P. Neff, Jr, Basic Electromagnetic Fields. 2nd Ed., New York, N.Y.: John Wiley & Sons, 1987.

[3] M. P. Morse and H. Feshbach, Methods of Theoretical Physics. Volume I., McGraw-Hill Book Company, 1953.

[4] W. R. Smythe, Static and Dynamic Electricity. 3rd Ed. Taylor and Francis Publishers, Inc., 1989.

[5] P. Moon, and D. E. Spencer, "Cylindrical and Rotational Coordinate Systems," Journal of the Franklin Institute, vol. 252, pp. 327-344, October 1951.

[6] P. Moon, and D. E. Spencer, "Separability Conditions for the Laplace and Helmholtz Equations," Journal of the Franklin Institute, vol. 253, pp. 586-600, 1952.

[7] P. Moon, and D. E. Spencer, Field theory for Engineers. 1st Ed., The Van Nostrand Series in Electronics and Communication, Ed. H. J. Reich. Princeton, New Jersey: D. Van Nostrand Company, Inc., 1961.

[8] C. Gao, F. Duewer, and X. D. Xiang, "Quantitative Microwave Evanescent Microscopy," Appl. Phys. Lett., vol. 75, no.19, pp. 3005-3009, 1999.

[9] E. Durand, Electrostatic Tomb II. Problemes Generaux Conducteurs. Paris, France: Masson and Son Publishers, 1966.

[10] R.A. Kleismit, G. Kozlowski, R.R. Biggers, I. Maartense, M.K. Kazimierczuk and D.B. Mast, "Characterization of local dielectric properties of superconductor $YBa_2Cu_3O_{7-\delta}$

using evanescent microwave microscopy," IEEE Trans.Appl.Supercond., vol.15, pp.2915-2918, 2005.

[11] R. B. Adler, Electromagnetic Energy Transmission and Radiation. New York, N.Y.: John Wiley & Sons, 1960.

[12] J. A. Kong, A. W. Morganthaler, and D. H. Staelin, Electromagnetic Waves. Englewood Cliffs, New Jersey: Prentice Hall, pp.365-369, 1991.

[13] R. A. Kleismit, M.K Kazimierczuk., G. Kozlowski, “Sensitivity and resolution of evanescent microwave microscope,” IEEE Trans. Microwave Theory and Technique., vol. 54, issue 2, part1, pp. 639 – 647, 2006.

[14] M. Tabib-Azar, D. Akinwande, G. E. Ponchak, and S. R. LeClair, "Evanescent microwave probes on high-resistivity silicon and its application in characterization of semiconductors," Rev. Sci. Instrum., vol.70, no. 7, pp. 3083-3086, 1999.

[15] M. Tabib-Azar, D. Akinwande, "Real-time imaging of semiconductor space-charge regions using high-spatial resolution evanescent microwave microscope," Rev. Sci. Instrum., vol. 71, no. 3, pp. 1460-1465, 1999.

[16] D. M. Pozar, Microwave Engineering. 2nd Ed., New York, N.Y.: John Wiley & Sons, 1998.

3 Theory for Measuring Local Complex Permittivity of Organic Materials Using Evanescent Microwave Microscopy

3.1 Introduction

The designs of microwave near-field probes utilizing coaxial resonators have been published by [1-3]. These coaxial resonator probes are classified as open-ended and the near-field consists of evanescent and propagative wave modes. This increases the difficulty of quantitative analysis, since both near-field and far-field interactions have to be considered in this case. This problem was resolved by shielding the open end of the resonator with an end wall aperture [4, 5]. The end-wall aperture is sized to cutoff for the frequency band of use and the propagative wave, exciting resonance within the probe is confined to the coaxial resonator structure. The probe tip extends through the shielding aperture and evanescent waves emanating from the tip interact with the sample properties. The tip of the probe operates in close proximity of the sample, where the tip radius and effective field distribution range are much smaller than the resonator excitation wavelength. The dynamic nature of the propagating field that excites resonance in the probe can be ignored, and the probe tip-sample field interaction can be treated as quasi-static. This will result in localized measurements and images with resolved features governed essentially by the characteristic size of the tip.

In performing quantitative measurements of different material properties, such as complex permittivity, the solution to a detailed electrostatic field configuration existing outside the tip is required. The probe tip and sample must be considered as a whole, and the solution of the electrostatic field equations at real boundary conditions and practical limits must be adhered

to in obtaining the perturbed field distributions. This will generate a methodology that explicitly relates the tip-sample distance to resonant frequency and Q shift of the resonator and physical material properties for a given geometry of the probe. The objective of this study is to represent a quantitative relationship between the real and imaginary parts of the local dielectric constant through the resonant frequency and quality factor shift using the method of images, resulting in a model applicable to measuring dielectric constant and loss of biological materials and providing quantitative results. This is accomplished by the derivation of the total perturbed electric field exterior to the tip presented in Section 3.2, in conjunction with the perturbed electric field equation within the sample.

3.2 Theoretical Analysis

3.2.1 Introduction

To quantitatively analyze organic dielectric materials, an analysis incorporating the method of images can be applied [3,5]. The resonator tip is represented as a charged conducting sphere with potential V_0 and when closely placed over a dielectric material it will be polarized by the electric field. This dielectric reaction to the tip causes a redistribution of charge on the tip in order to maintain the equipotential surface of the sphere and also results in a shift in frequency and Q of the resonator. Applying the method of images to model the field redistribution requires a series of image charges in an iterative process to meet boundary conditions at probe tip and dielectric sample surface as shown in figure 3.1.

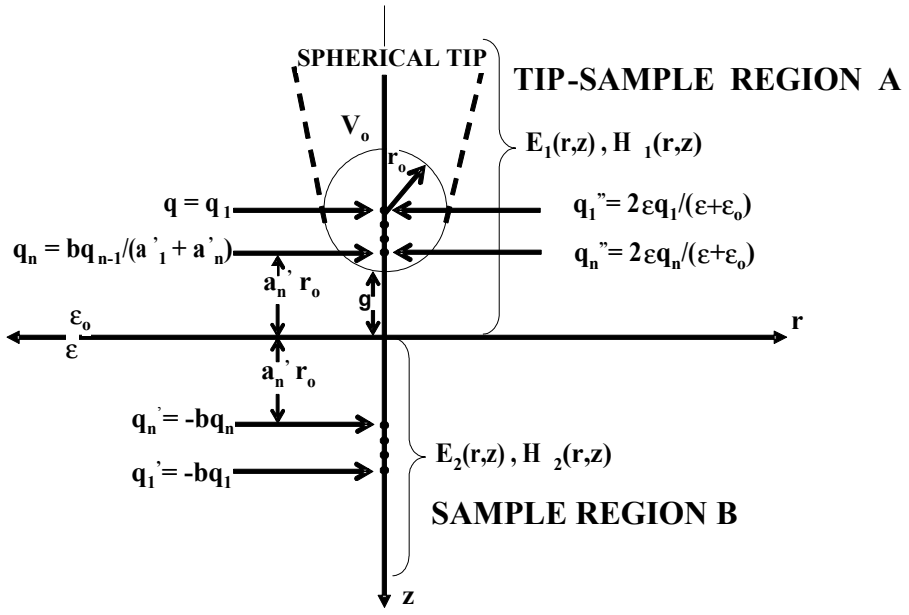

Fig. 3.1. Image charges (q, q', q") for a spherical tip above a sample [5].

3.2.2 Theoretical Model for Resonant Frequency – Two Point Method

The expression for the resonant frequency shift due to the presence of a material is

$$\frac{\Delta f}{f} = -\frac{\int_V (\Delta\varepsilon)(\overline{E}_0^* \cdot \overline{E}) + (\Delta\mu)(\overline{H}_0^* \cdot \overline{H})dV}{\int_V (\varepsilon_0 \overline{E}_0^2 + \mu_0 \overline{H}_0^2)dV} = \frac{f - f_0}{f}, \tag{3.1}$$

$$= \frac{1}{U} \cdot \int_V \left((\Delta\varepsilon)\left(\overline{E}_0^* \cdot \overline{E}\right) + (\Delta\mu)\left(\overline{H}_0^* \cdot \overline{H}\right)\right)dV$$

where $U = \int_V (\varepsilon_0 \overline{E}_0^2 + \mu_0 \overline{H}_0^2)dV$ is the total unperturbed electromagnetic energy, $\overline{E}, \overline{H}$ is the perturbed electric and magnetic fields, $\overline{E}_0, \overline{H}_0$ is the unperturbed fields, V is the volume of a region outside the resonator tip, f is the resonant frequency, and f_0 is the unperturbed reference frequency. The unperturbed electric field $\overline{E}_0$ is found by taking the negative gradient of the potential φ_0 due to charge q.

$$-\nabla\varphi_0 = \frac{q}{4\pi\varepsilon_0}\frac{\left[r\hat{r}+\left(z+r_0+g\right)\hat{z}\right]}{\left[r^2+\left(z+r_0+g\right)^2\right]^{3/2}} = \overline{E}_0(r,z), \tag{3.2}$$

where r_0 is tip radius and g is a distance from tip to the surface of the sample. Substituting $\alpha = a_1' r_0 = r_0 + g, a_1' = 1 + g/r_0$ into Eq. (3.2) results in

$$\overline{E}_0(r,z) = \frac{q}{4\pi\varepsilon_0}\frac{\left[r\hat{r}+\left(z+\alpha\right)\hat{z}\right]}{\left[r^2+\left(z+\alpha\right)^2\right]^{3/2}}. \tag{3.3}$$

The potential V_0 on the surface of the spherical tip is given by

$$V_0 = \frac{q}{4\pi\varepsilon_0 r_0} \tag{3.4}$$

By using the method of images (figure 3.1) the perturbed electric field within the sample E_B can be derived similar to the unperturbed field using an iterative method and is given by

$$\overline{E}_B(r,z) = \frac{1}{2\pi(\varepsilon+\varepsilon_0)}\sum_{n=1}^{\infty} q_n \frac{\left[r\hat{r}+\left(z+\beta\right)\hat{z}\right]}{\left[r^2+\left(z+\beta\right)^2\right]^{3/2}}, \tag{3.5}$$

where

$$\beta = a_n' r_0,\ a_n' = a_1' - \frac{1}{a_1'+a_{n-1}'},\ q_n = t_n q,\ t_n = \frac{b t_{n-1}}{a_1'+a_{n-1}'},\ t_1 = 1, \text{ and } b = \frac{\varepsilon-\varepsilon_0}{\varepsilon+\varepsilon_0}. \tag{3.6}$$

The perturbed electric field $\overline{E}_A$ in the tip-sample region A is derived similar to Eq.(3.5) and is written as

$$\overline{E}_A(r,z) = \frac{1}{4\pi\varepsilon_0}\sum_{n=1}^{\infty} q_n \left[\frac{\left[r\hat{r}+\left(z+a_n' r_0\right)\hat{z}\right]}{\left[r^2+\left(z+a_n' r_0\right)^2\right]^{3/2}} - b\frac{\left[r\hat{r}+\left(z-a_n' r_0\right)\hat{z}\right]}{\left[r^2+\left(z-a_n' r_n\right)^2\right]^{3/2}}\right] \tag{3.7}$$

It is important to notice that for a tip placed in free space $\varepsilon = \varepsilon_0$ at the location, $r = 0$ and $z = -g - r_0 = -a_1 r_0$ and $\overline{E}_0$ is equal to $\overline{E}_A$ and $\overline{E}_B$, see Eqs. (3.3), (3.5) and (3.7). By

integrating the unperturbed Eq. (3.3) and the perturbed electric fields Eq. (3.5) and Eq. (3.7) over a region V outside the spherical tip, the total relative frequency shift becomes

$$\left(\frac{\Delta f}{f}\right)_A = -C\sum_{n=1}^{\infty} t_n\left\{1-\frac{1}{2}(1+b)\frac{1}{a_1'+a_n'}\right\}, \text{ Region A,} \tag{3.8}$$

$$\left(\frac{\Delta f}{f}\right)_B = -\left(\frac{\Delta\varepsilon}{E}\right)\frac{(4\pi\varepsilon_0)r_0V_0^2}{(\varepsilon+\varepsilon_0)}\sum_{n=1}^{\infty}\frac{t_n}{(a_n'+a_n')} = -C\sum_{n=1}^{\infty}\frac{bt_n}{(a_1'+a_n')}, \text{ Region B,} \tag{3.9}$$

where C is a geometry factor of the tip-resonator assembly.

The summation of Eq.(3.8) and Eq.(3.9) results in the over all resonant frequency shift due to the perturbed electric fields in both regions

$$\left(\frac{\Delta f}{f}\right)_{total} = \left(\frac{\Delta f}{f_0}\right)_{A+B} = -C\sum_{n=1}^{\infty} t_n\left\{1-\frac{1}{2}(1-b)\frac{1}{a_1'+a_n'}\right\}. \tag{3.10}$$

Taking into account the real part of Eq. (3.10), we can fit analytical expression to our experimental data to find the complex dielectric constant. The real and imaginary component of permittivity and resonant frequency change when the tip touches the sample can be easily obtained. Specifically, when $g = 0$ the resonant frequency shift is given by

$$\left(\frac{\Delta f}{f}\right)_{total} = -C\sum_{n=1}^{\infty} t_n\left(1-\frac{1}{2}(1-b)\frac{1}{a_1'+a_n'}\right) \tag{3.11}$$

$$= -C\sum_{n=1}^{\infty}\frac{b^{n-1}}{n}\left(1-\frac{1}{2}(1-b)\left(\frac{n}{n+1}\right)\right)$$

$$= C\left(\frac{\ln(1-b)}{b}-\frac{(1-b)}{2b}-\frac{(1-b)}{2b^2}\ln(1-b)\right)$$

By expressing

$$\ln(1-b) = -\sum_{k=1}^{\infty}\left(\frac{b^k}{k}\right)$$

and

$$b = R\exp(i\phi),$$

where

$$R = \left((\varepsilon'^2 + \varepsilon''^2 - 1)^2 + 4\varepsilon''^2\right)^{1/2} / \left((\varepsilon' + 1)^2 + \varepsilon''^2\right) \text{ and}$$

$$\phi = \tan^{-1}\left((2\varepsilon'\varepsilon'')/\left(\varepsilon'^2 + \varepsilon''^2 - 1\right)\right)$$

from Eq. (3.11) the real and imaginary parts of the relative resonant frequency shift is

$$\left(\frac{\Delta f}{f}\right)_{total} = \frac{C}{2}\left(1 - \frac{1}{b} + \sum_{k=1}^{\infty}\frac{1}{k}(b^{k-2} - 3b^{k-1})\right)$$

$$\left(\frac{\Delta f}{f}\right)_{total} = \left(\frac{\Delta f}{f}\right)_{real} + i\left(\frac{\Delta f}{f}\right)_{imaginary}$$

$$= \frac{C}{2}\left(1 + \frac{\cos\varphi}{R} + \sum_{k=1}^{\infty}\frac{1}{k}(R^{k-2}\cos((k-2)\varphi) - 3R^{k-1}\cos((k-1)\phi))\right)$$

$$+ \frac{iC}{2}\left(1 + \frac{\sin\varphi}{R} + \sum_{k=1}^{\infty}\frac{1}{k}(R^{k-2}\sin((k-2)\varphi) - 3R^{k-1}\sin((k-1)\phi))\right)$$

Therefore, when the tip touches the sample at g = 0

$$\left(\frac{\Delta f}{f}\right)_{real} = \frac{C}{2}\left(1 - \frac{\cos\varphi}{R} + \sum_{k=1}^{\infty}\frac{1}{k}(R^{k-2}\cos((k-2)\varphi) - 3R^{k-1}\cos((k-1)\phi))\right) \quad (3.12)$$

The local dielectric properties of the materials are described by a complex permittivity $\varepsilon' + i\varepsilon''$. The parameter ε'' is the local conductivity described by the well-known equation $\varepsilon = \varepsilon' + i\sigma/(\omega\varepsilon_0)$ where ε' is the relative dielectric constant, $\varepsilon'' = \sigma/\omega\varepsilon_0$, σ is the conductivity, ω is the angular frequency, and ε_0 is the permittivity of free space.

By using two fundamental Maxwell equations exclusive of and in the presence of the material we can derive an expression for the perturbed frequency of the resonator f, which is different from unperturbed frequency f_0.

$$\begin{aligned}
&\overline{\nabla}\times\overline{E}_0 = -i\,\omega_0\mu_0\overline{H}_0\\
&\overline{\nabla}\times\overline{E} = -i\,\omega\ \overline{H}\\
&\overline{\nabla}\times\overline{H}_0 = i\,\omega_0\mu_0\overline{E}_0\\
&\overline{\nabla}\times\overline{H} = i\,\omega\ \overline{E}
\end{aligned} \qquad (3.13\text{-}3.16)$$

Through straightforward manipulations of Eqs. (3.13) - (3.16) we have

$$\overline{\nabla}\cdot(\overline{E}_0^*\times\overline{H}) = i\omega_0\mu_0\overline{H}_0^*\cdot\overline{H} - i\omega\omega\mu\overline{E}_0^*\cdot\overline{E}\quad , \qquad (3.17)$$

$$\overline{\nabla}\cdot(\overline{E}\times\overline{H}_0^*) = -i\omega\mu\overline{H}_0^*\cdot\overline{H} + i\omega_0\,\mu_0\,\overline{E}_0^*\cdot\overline{E}\quad , \qquad (3.18)$$

$$\int_V\nabla\cdot(\overline{E}_0^*\times\overline{H}+\overline{E}\times\overline{H}_0^*)dV = \oint_S(\overline{E}_0^*\times\overline{H}+\overline{E}\times\overline{H}_0^*)dS = 0 =$$

$$i\int_V[(\omega_0\varepsilon_0-\omega\varepsilon)\overline{E}_0^*\cdot\overline{E}+(\omega_0\mu_0-\omega\mu)\overline{H}_0^*\cdot\overline{H}]dV \qquad (3.19)$$

which allows us to arrive at the final expression for f

$$\frac{\omega}{\omega_0} = \frac{\int_V(\varepsilon_0\overline{E}_0^*\cdot\overline{E}+\mu_0\overline{H}_0^*\cdot\overline{H})dV}{\int_V(\varepsilon\overline{E}_0^*\cdot\overline{E}+\mu\overline{H}_0^*\cdot\overline{H})dV} = \frac{f}{f_0} \qquad (3.20)$$

Assuming that the magnetic fields are negligible with respect to their electric counterparts we can calculate these integrals analytically for the assumed geometry (Fig.3.1),

$$\int_V\varepsilon_0(\overline{E}_0^*\cdot\overline{E})dV = (qV_0)\sum_{n=1}^{\infty}t_n\left[1-\frac{1}{2}(1+b)\frac{1}{(a_1'+a_n')}+\frac{\varepsilon_0}{(\varepsilon+\varepsilon_0)}\frac{1}{(a_1'+a_n')}\right], \qquad (3.21)$$

$$\int_V\varepsilon(\overline{E}_0^*\cdot\overline{E})dV = (qV_0)\sum_{n=1}^{\infty}t_n\left[1-\frac{1}{2}(1+b)\frac{1}{(a_1'+a_n')}+\frac{\varepsilon}{(\varepsilon+\varepsilon_0)}\frac{1}{(a_1'+a_n')}\right], \qquad (3.22)$$

which leads to a straightforward expression for frequency f

$$\frac{f}{f_0} = \frac{\sum_{n=1}^{\infty}(t_n - t_{n-1})}{\sum_{n=1}^{\infty}(t_n)} = \frac{1}{\sum_{n=1}^{\infty}(t_n)} \quad . \tag{3.23}$$

Before going to the physical interpretation of the above analytical results let us compare our two expressions for frequency, namely, Eq. (3.1) – approximated and Eq. (3.20) – exact. By rearranging Eq. (3.20) we have

$$\frac{\Delta f}{f} = \frac{f - f_0}{f} = 1 - \frac{f_0}{f} = \frac{\int_V (\Delta \overline{E}_0^* \cdot \overline{E} + \Delta\mu \overline{H}_0^* \cdot \overline{H}) dV}{\int_V (\varepsilon \overline{E}_0^* \cdot \overline{E} + \mu \overline{H}_0^* \cdot \overline{H}) dV} \tag{3.24}$$

To get Eq. (3.1) from Eq. (3.24) it required to assume that due to the presence of the sample only a small perturbation of the electromagnetic field takes place resulting in replacement of $\overline{\mathrm{E}}$ by $\overline{\mathrm{E}}_0$ and $\overline{\mathrm{H}}$ by $\overline{\mathrm{H}}_0$ in the denominator of Eq. (3.24). A general case where g ≈ 0 and the sample has arbitrary electromagnetic properties, from

$$\left(\frac{\Delta f}{f}\right) = -\sum_{n=1}^{\infty} \frac{b^n}{(n+1)} \left[1 - \frac{(n+1)^2}{3} a'\right] \tag{3.25}$$

with $a' = g / r_0$ or

$$\frac{f}{f_0} = 1 + \sum_{n=1}^{\infty} \frac{b^n}{(n+1)} - \frac{1}{3} a' \sum_{n=1}^{\infty} (n+1) b^n \, . \tag{3.26}$$

Summing up Eqs. (3.25) and (3.26) into analytical form, we have

$$\left(\frac{\Delta f}{f}\right) = 1 + \frac{\ln(1-b)}{b} + a' \frac{b(2-b)}{3(1-b)^2} \qquad \text{or} \tag{3.27}$$

$$\left(\frac{f}{f_0}\right) = -\frac{b}{\ln(1-b)} + a'\frac{b^3(2-b)}{3(1-b)^2[\ln(1-b)]^2}. \tag{3.28}$$

From Eq. (3.28) we can derive two experimentally important expressions; the resonant frequency and the associated slope at g = 0 (or a′ = 0):

$$\text{frequency} \quad f(g=0) = -\frac{b}{\ln(1-b)} f_0 \tag{3.29}$$

$$\text{slope} \quad \frac{df}{dg}(g=0) = \left(\frac{f_0}{r_0}\right)\frac{b^3(2-b)}{3(1-b)^2[\ln(1-b)]^2} \tag{3.30}$$

In equations (3.29) and (3.30), the right hand sides are complex because of $b = (\varepsilon' - i\varepsilon'' - 1)/(\varepsilon' - i\varepsilon'' + 1)$. The real part of the complex expression on the right side of Eqs. (3.29) and (3.30) has to be calculated in order to compare them with experimental data.

3.2.3 Theoretical Model for Resonant Quality Factor – Two Point Method

The theory applied for a microwave resonator deals only with the field distributed outside the tip including a sample space. The fundamental assumption of the theory is that the presence of the material introduces a perturbation to the existing electromagnetic field distribution. The expression for the resonant frequency change and a reciprocal change of quality factor is described by the following expressions

$$-2\frac{\Delta f}{f} - i\Delta\left(\frac{1}{Q}\right) = \frac{\int_V (\Delta\varepsilon^* \overline{E}_0^* \cdot \overline{E} + \Delta\mu \overline{H}_0^* \cdot \overline{H})dV}{\int_V (\varepsilon^* \overline{E}_0^* \cdot \overline{E} + \mu \overline{H}_0^* \cdot \overline{H})dV} \tag{3.31}$$

$$\frac{\Delta f}{f} = \frac{(f - f_0)}{f} \tag{3.32}$$

$$\Delta\left(\frac{1}{\mathrm{Q}}\right)=\frac{1}{Q}-\frac{1}{Q_0} \tag{3.33}$$

where $\overline{\mathrm{E}}_0$ and $\overline{\mathrm{H}}_0$ are the unperturbed electric and magnetic fields, $\vec{\mathrm{E}}$ and $\vec{\mathrm{H}}$ are the perturbed fields, V is the volume of a region outside the resonator tip, f and Q are the perturbed resonant frequency and quality factor and f_0 and Q_0 are the reference (or unperturbed) resonant frequency and quality factor, respectively. The unperturbed field is given by

$$\overline{E}_0(r,z)=\frac{q}{4\pi\varepsilon_0}\frac{\left[r\hat{r}+\left(z+\alpha\right)\hat{z}\right]}{\left[r^2+\left(z+\alpha\right)^2\right]^{3/2}} \tag{3.34}$$

where $\alpha=a_1'r_0=r_0+g, a_1'=1+g/r_0$ with radius of the spherical tip r_0 and with g as the gap between the tip and surface of the sample. The potential V_0 on the surface of the spherical tip is given by

$$V_0=\frac{q}{4\pi\varepsilon_0 r_0}\ . \tag{3.35}$$

By using the method of image (figure 3.1), the perturbed electric field in the tip-sample region (region A) and the sample volume (region B) respectively is described by the following analytical formulas (where r_0 is much smaller than the sample thickness)

$$\overline{E}_A(r,z)=\frac{1}{4\pi\varepsilon_0}\sum_{n=1}^{\infty}q_n\left[\frac{\left[r\hat{r}+\left(z+a_n'r_0\right)\hat{z}\right]}{\left[r^2+\left(z+a_n'r_0\right)^2\right]^{3/2}}-b\frac{\left[r\hat{r}+\left(z-a_n'r_0\right)\hat{z}\right]}{\left[r^2+\left(z-a_n'r_n\right)^2\right]^{3/2}}\right] \tag{3.36}$$

$$\overline{E}_B(r,z)=\frac{1}{2\pi\left(\varepsilon^*+\varepsilon_0\right)}\sum_{n=1}^{\infty}q_n\frac{\left[r\hat{r}+\left(z+\beta\right)\hat{z}\right]}{\left[r^2+\left(z+\beta\right)^2\right]^{3/2}} \tag{3.37}$$

where

$$\beta = a_n' r_0,\ a_n' = a_1' - \frac{1}{a_1' + a_{n-1}'},\ q_n = t_n q,\ t_n = \frac{b t_{n-1}}{a_1' + a_{n-1}'},\ t_1 = 1$$

$$b = \frac{\varepsilon^* - \varepsilon_0}{\varepsilon^* + \varepsilon_0},\ \varepsilon^* = \varepsilon'^* + i\varepsilon''^*, \text{and } \Delta\varepsilon^* = \varepsilon^* - \varepsilon_0 \tag{3.38}$$

It is important to notice that for a tip placed in free space $\varepsilon = \varepsilon_0$ at the location, $r = 0$ and $z = -g - r_0 = -a_1 r_0$ and $\overline{E}_0$ is equal to $\overline{E}_A$ and $\overline{E}_B$, see Eqs. (3.34), (3.36) and (3.37). By integrating the unperturbed Eq.(3.34) and the perturbed electric fields Eq. (3.36) and Eq. (3.37) over a region V outside the spherical tip and assuming for simplicity that magnetic fields are negligible with respect to their electric counterparts we are in position to calculate analytically integrals on the right side of Eq. (3.31) for assumed geometry (figure 3.1)

$$\int_V \varepsilon_0 (\overline{E}_0^* \cdot \overline{E}) dV = (qV_0) \sum_{n=1}^{\infty} t_n \left[1 - \frac{1}{2}(1+b) \frac{1}{a_1' + a_n'} + \frac{\varepsilon_0}{(\varepsilon^* + \varepsilon_0)} \frac{1}{(a_1' + a')} \right], \tag{3.39}$$

$$\int_V \varepsilon_0 (\overline{E}_0^* \cdot \overline{E}) dV = (qV_0) \sum_{n=1}^{\infty} t_n \left[1 - \frac{1}{2}(1+b) \frac{1}{a_1' + a_n'} + \frac{\varepsilon^*}{(\varepsilon^* + \varepsilon_0)} \frac{1}{(a_1' + a')} \right], \tag{3.40}$$

leading to the straightforward expression for Eq. (3.31)

$$-2\frac{\Delta f}{f} - i\Delta\left(\frac{1}{Q}\right) = \frac{\int_v (\Delta\varepsilon^* \overline{E}_0^* \cdot \overline{E} + \Delta\mu \overline{H}_0^* \cdot \overline{H}) dV}{\int_v (\varepsilon^* \overline{E}_0^* \cdot \overline{E} + \mu \overline{H}_0^* \cdot \overline{H}) dV} = \sum_{n=1}^{\infty} b^n \left(\prod_{k=1}^{n} \frac{1}{(a_1' + a_k')} \right) \tag{3.41}$$

The right hand side of Eq. (3.41) is a complex number with respect to the local complex permittivity describing dielectric and conductive properties of the materials. This can be done

for a general case, but our discussion is restricted to when the tip touches the sample. Specifically, using Eq. (3.38), we can show that

$$\sum_{n=1}^{\infty} b^n \left(\prod_{k=1}^{n} \frac{1}{(a_1' + a_k')} \right) = -1 - \frac{\ln(1-b)}{b} \tag{3.42}$$

and

$$\frac{\Delta f}{f} = \frac{1}{2} \mathrm{Re}\left[1 + \frac{\ln(1-b)}{b} \right] \tag{3.43}$$

$$\Delta\left(\frac{1}{Q} \right) = -\mathrm{Im}\left[1 + \frac{\ln(1-b)}{b} \right] \tag{3.44}$$

The Eqs. (3.43)-(3.44) may be rearranged into more appropriate forms assuming that we know experimentally f_0 and Q_0.

$$f = \frac{f_0}{\left[1 + \frac{1}{2} \mathrm{Re}\left(\frac{b}{2} + \frac{b^2}{3} + \ldots \right) \right]} \tag{3.45}$$

$$Q = \frac{Q_0}{\left[1 + \frac{1}{2} Q_0 \, \mathrm{Im}\left(\frac{b}{2} + \frac{b^2}{3} + \ldots \right) \right]} \tag{3.46}$$

and

$$b = \frac{\varepsilon_1 - 1 - i\varepsilon_2}{\varepsilon_1 + 1 - i\varepsilon_2}, \varepsilon_2 = \frac{\varepsilon''}{\varepsilon_0} = \frac{\sigma}{\omega \varepsilon_0}, \varepsilon_1 = \frac{\varepsilon'}{\varepsilon_0}. \tag{3.47}$$

By using Eq. (3.46), the approximated expression for the perturbed resonant frequency and quality factor at $g = 0$ has the following forms given in Eqs. (3.48) and (3.49) respectively:

$$f(g=0)=\frac{f_0}{1+\frac{1}{2}\left[\frac{1}{2}\frac{\alpha}{\beta}+\frac{1}{3}\frac{\alpha^2-4\varepsilon_2^2}{\beta^2}+\frac{1}{4}\frac{\alpha(\alpha^2-12\varepsilon_2^2}{\beta^3}+\ldots\right]} \tag{3.48}$$

$$Q(g=0)=\frac{Q_0}{1+Q_0\left(\frac{\varepsilon_2}{\beta}\right)\left[1+\frac{4\alpha}{3\beta}+\frac{3\alpha^2-4\varepsilon_2^2}{2\beta^2}+\ldots\right]} \tag{3.49}$$

where $\alpha=\varepsilon_1^2+\varepsilon_2^2-1,\ \beta=(\varepsilon_1+1)^2+\varepsilon_2^2.$ (3.50)

The infinite summation in Eqs.(3.45)-(3.46) are divergent to the following analytical formulas

$$f(g=0)=\frac{f_0}{1-\frac{1}{2}-\frac{x\ln\sqrt{(1-x)^2+y^2}-y\arctan\frac{y}{(1-x)}}{2(x^2+y^2)}} \tag{3.51}$$

$$Q(g=0)=\frac{Q_0}{1+Q_0\frac{x\arctan\frac{y}{(1-x)}+y\ln\sqrt{(1-x)^2+y^2}}{x^2+y^2}} \tag{3.52}$$

3.2.4 Theoretical Model – Multi-Point Method

The multi-point method is used when the probe tip is not in contact with the sample under interrogation. If we start with Eq. (3.9), which has been repeated below for convenience and again referring to figure (3.1) the real part of (3.9) can be calculated by

$$\left(\frac{\Delta f}{f}\right)_{total}=\left(\frac{\Delta f}{f_0}\right)_{\mathrm{A+B}}=-C\sum_{n=1}^{\infty}t_n\left\{1-\frac{1}{2}(1-b)\frac{1}{a_1'+a_n'}\right\} \tag{3.9}$$

defining the summation of the real and imaginary parts of term *b* as follows

$$\frac{1}{2}(b^n + b^{*n}) = \frac{S^n}{2}(e^{in\varphi} + e^{-in\varphi}) = S^n \cos n\varphi \quad . \tag{3.53}$$

The parameters $S, \varphi,$ and b^* are defined in [5]. By taking into account the real part of expression (3.9), we obtain the following expression, which is used to compare with the experimental data [3, 5].

$$\left(\frac{\Delta f}{f_0}\right)_{total}^{real} = -\frac{C}{2}\sum_{n=1}^{\infty}\left\{S^n\left[\cos n\varphi\right]\left(\prod_{k=1}^{n}\frac{1}{a_1' + a_k'}\right)\right\} - C\left(1 - \frac{1}{4a_1'}\right)$$
$$- C\sum_{n=2}^{\infty}\left\{S^{n-1}\left[\cos(n-1)\varphi\right]\left(\prod_{k=2}^{n}\frac{1}{a_1' + a_{k-1}'}\right)\left(1 - \frac{1}{2(a_1' + a_n')}\right)\right\} \tag{3.54}$$

3.3 Measurement Procedure Multi-point Method

The microscope probe consists of a tuned, end wall apertured coaxial transmission line. The resonator probe is coupled to the network analyzer through the tuning network and coupled to the sample. When the resonator tip is in close proximity of the sample, the resonant frequency of the resonator *f* will shift. In measuring the resonant frequency shift, the resonant frequency reference of the probe is set at a fixed distance above the sample. The distance between probe tip and sample is sufficient to assure that the evanescent field emanating from the tip will not interact with the sample where this distance or decay length is governed by the aperture size. The field distribution from the probe tip extends outward a short distance with the amplitude of the evanescent field decaying exponentially, as a material is entered into the near field of the probe, it will interact with the evanescent field, perturbing it. This will result in the loading of the resonator via the coupling and is considered part of the resonant circuit resulting in losses added to the system, which will decrease the microscope resonant frequency. The measured resonant frequency shift vs. tip-

sample separation g will generate a transfer function relating the change in resonant frequency of the resonator Δf to tip-sample separation Δg as a function of complex permittivity of the sample, which is best fit with an electrostatic field model generated from the method of images (3.53) to extract the complex permittivity values. To establish the reference frequency f_0, the height of the probe tip above the surface of the sample was set a few microns beyond the decay length of the evanescent field at the desired frequency. The probe tip is then indexed down toward the tissue sample, but never touching it and the corresponding shift in resonant frequency of the resonator was recorded for each indexed position. The measurement of a resonant frequency f vs. tip-sample standoff height g, generates a raw data curve, that is fit by model equation (3.53), using three fitting parameters. The fit parameters of the model consist of: geometry factor C and reduced complex permittivity $\frac{\varepsilon'}{\varepsilon_0}, \frac{\varepsilon''}{\varepsilon_0}$.

3.4 Measurement Procedure Two-point Method

Eqs. (3.47)-(3.48) can be used to calculate the total shift in frequency and in Q to determine the real and imaginary components respectively of the local complex dielectric constant sensed by the probe tip. The total shift is comprised of a resonant frequency f_0 and Q_0 when the probe is not influenced by a material (unperturbed) in its near field and is due to its own self resonance. The material is then brought into the near field of the probe and touches the tip (perturbed), resulting in a total shift in frequency to f and Q which is analytically determined between f_0, f and Q_0, Q to determine the localized complex permittivity parameters. The tissue samples are soft enough allowing the tip to touch the surface without damaging the probe, making the device unique for characterizing biological

samples.

3.5 Results

The multi-point and two point measurement methods were conducted on freshly excised porcine tissue at identical locations in order to compare quantitative results. Figure 3.2 is representative of the raw frequency shift data (circles) and multi-point model fit with Eq. (3.53) resulting in a dielectric constant value of 23.9 and dielectric loss of 17.0.

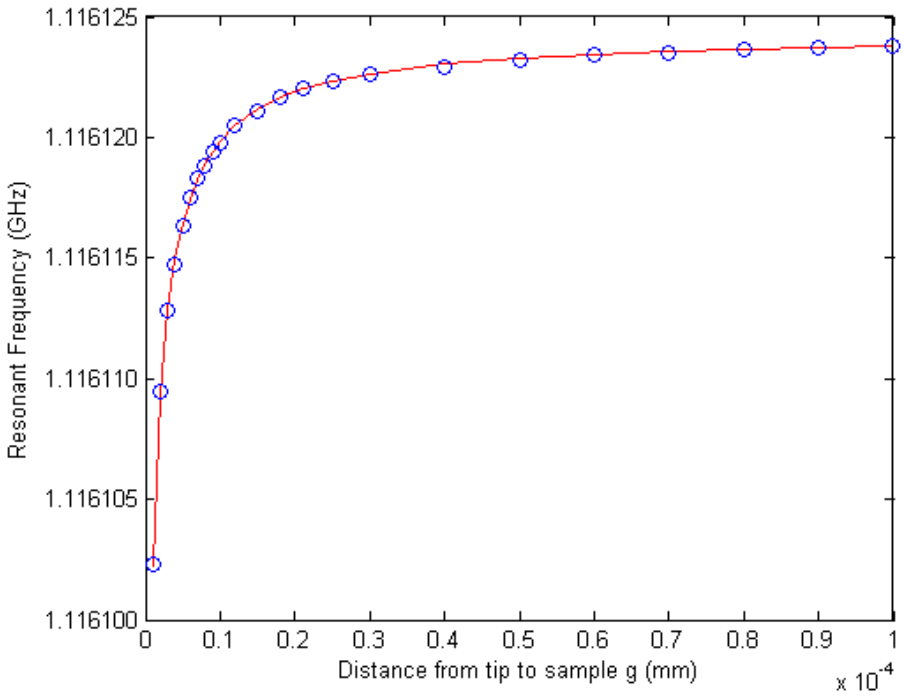

Fig. 3.2 Multi-point model fit of resonant Δf vs. Δg for porcine skin tissue sample.

Figures (3.3 and 3.4) show the two point method for determining dielectric constant and dielectric loss respectively, with the raw data depicted by circles and the calculation as a solid red line. The complex permittivity values for this method are 24.0 for dielectric constant and 17.0 for dielectric loss.

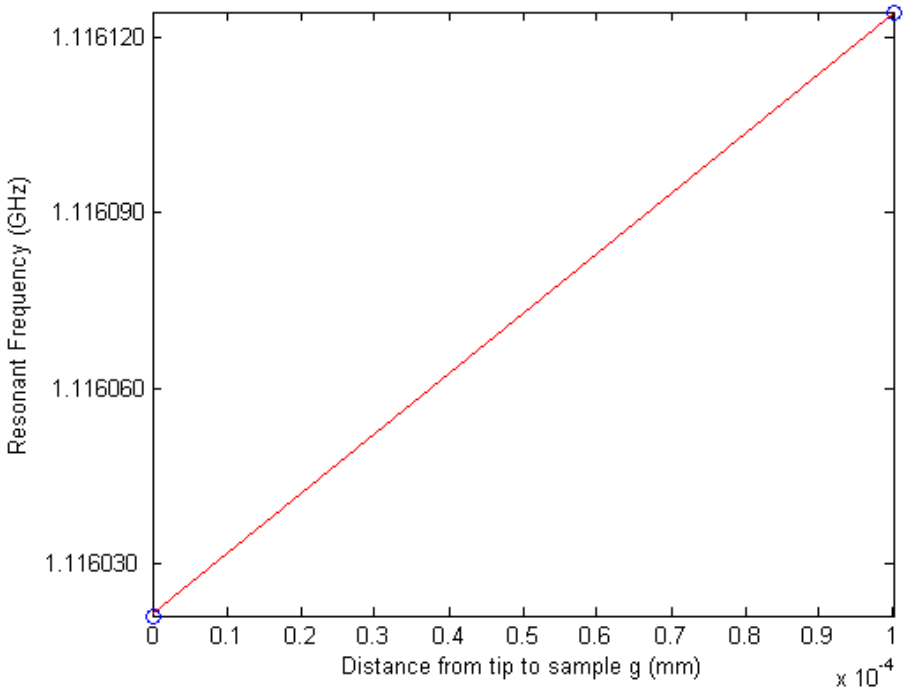

Fig. 3.3 Two point calculation of resonant Δf vs. Δg for porcine skin tissue sample.

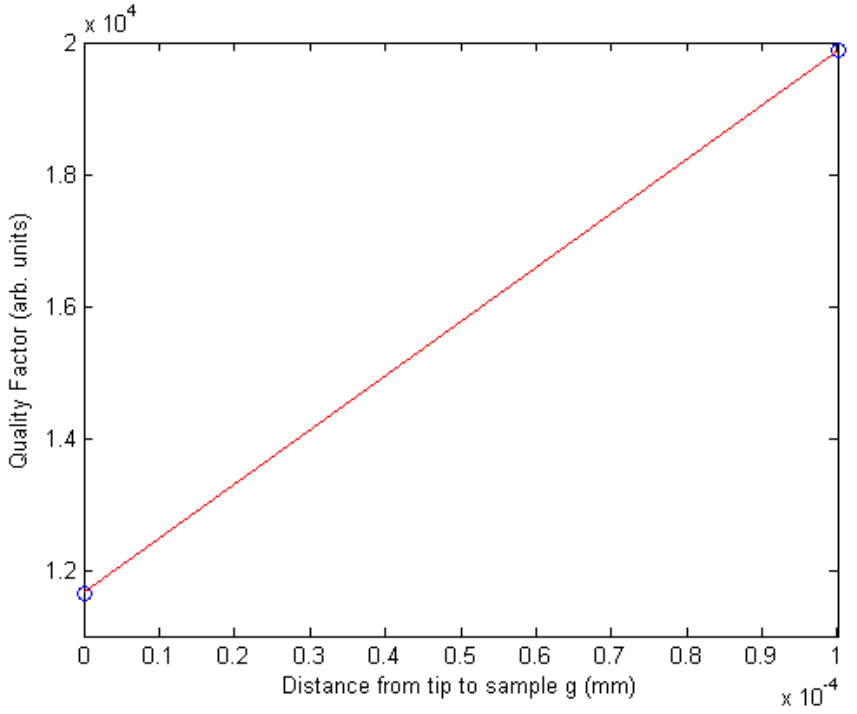

Fig. 3.4 Two point calculation of resonant ΔQ vs. Δg for porcine skin tissue sample.

3.6 Conclusion

The multi-point method utilizing equation (3.54) employs only frequency shift data to determine complex permittivity through an infinite series solution. A significant number of iterations are required to fit the experimental data and determine the complex permittivity values accurately. The probe tip does not touch the sample, when using this method and only approaches within one micron of the sample surface.

The two point method incorporating equations (3.48 and 3.49) to determine the complex permittivity values by linear fitting between the perturbed and unperturbed total shift states in frequency and quality factor of the resonator. These equations are highly asymptotic and converge rapidly and only require about 500 iterations to determine the permittivity parameters precisely. The two point method decreases the processing time required to suitably determine the electric parameters of a material and is only applicable to soft materials such as biological tissue. Both methods clearly produce comparable results, but the two point technique is superior in processing and testing time, but limited in material type.

3.7 Chapter 3 References

[1] G. Gao and X.-D. Xiang , "Quantitative microwave near-field microscopy of dielectric properties," Review of Scientific Instruments, vol. 69, pp. 3846-3851, Nov.1998.

[2] D. E. Steinhauer, C. P. Vlahacos, S. K. Dutta, B. J. Feenstra, F. C. Wellstood, and S. M. Anlage, "Quantitative imaging of sheet resistance with a scanning near-field microwave microscope," Appl. Phys. Lett., vol. 72, no.7, pp. 861-863, Feb. 1998.

[3] R. A. Kleismit, G. Kozlowski, R. R. Biggers, I. Maartense, M. K. Kazimierczuk, and D. B. Mast, "Characterization of local dielectric properties of superconductor

$YBa_2Cu_3O_{7-\delta}$ using evanescent microwave microscopy," *IEEE Trans. Appl. Supercond.,* vol. 15, pp. 2915-2918, July 2005.

[4] X .- D . Xiang and C. Gao, " Quantitative complex electrical impedance microscopy by scanning evanescent microwave microscope, *Materials Characterization*, vol. 48, pp. 117-125, Apr. 2002.

[5] R. A. Kleismit, M. ElAshry, G. Kozlowski, M. S. Amer, M. K. Kazimierczuk, and R. R. Biggers, "Local dielectric and strain measurements in $YBa_2Cu_3O_{7-\delta}$ thin films by evanescent microscopy and Raman spectroscopy," *Supercond. Sci. Technol.*, vol. 18, pp. 1197-1203, July 2005

4 Quantitative Evanescent Microwave Microscopy of Porcine Skin Tissue in the Frequency Range From 1 GHz to 15 GHz

4.1 Introduction

Microwave properties are a function of complex permittivity, permeability, and free carrier concentration. In most biological tissues, moisture content, ionic species such as Na^+ and K^+, free radicals, and iron content of blood serum affect the conductivity significantly. These parameters along with density variations, which affect the dielectric constant, can be mapped and quantified through evanescent microwave microscopy. A significant strength of the microwave evanescent field is its ability to penetrate depth-wise into a biological sample and sense localized quantitative material changes in-situ without the exponentially decaying field altering the sample properties.

The objective of this study is to utilize the evanescent microwave probe to investigate the complex permittivity of excised porcine skin tissue samples in the range of frequency from 1 GHz to 15 GHz. This investigation presents experimental results of probe scan images and specific local complex dielectric measurements of tissue lesions, surface burns, and histological tissue structures utilizing the evanescent microscopy system shown in figure 4.1. To our knowledge, no previous studies using microwave probe techniques have examined the dielectric properties of porcine skin with lesions or burns, or have attempted to correlate the dielectric properties and conductivity with histological tissue structures such as blood vessels or glandular ducts.

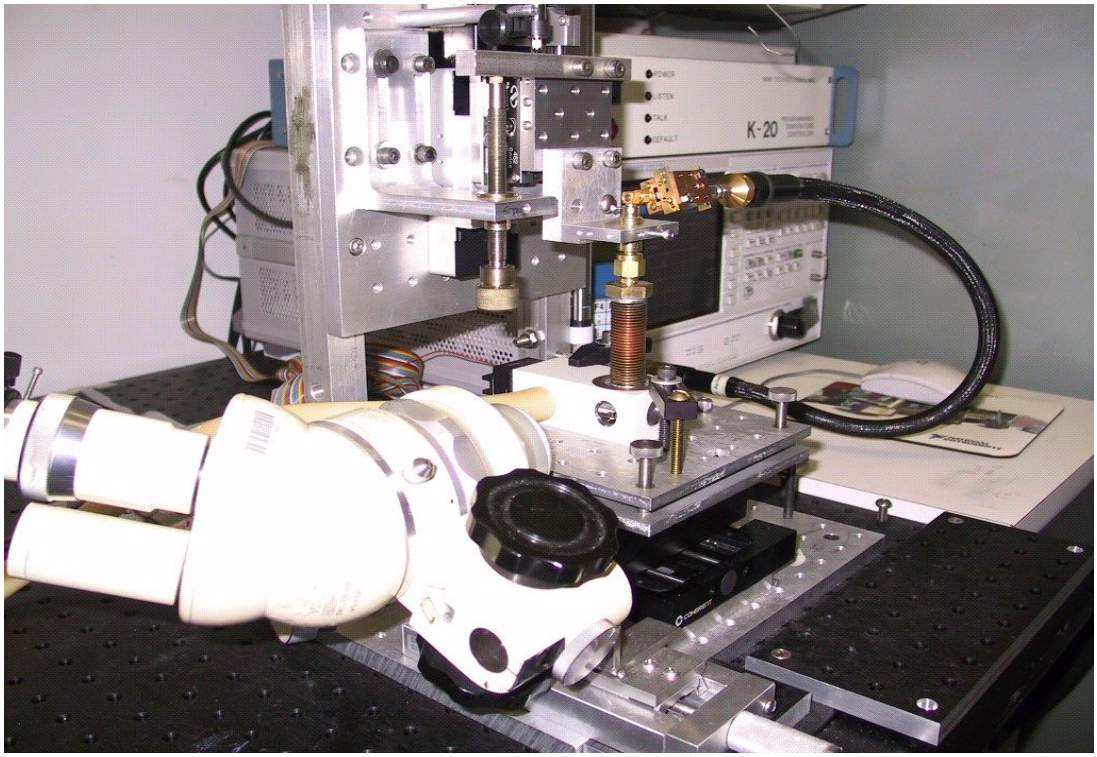

Fig. 4.1. Evanescent microwave microscopy system [1].

4.2 Measurement System

The tissue induced changes in the probe's resonant frequency, quality factor, and reflection coefficient are tracked by a Hewlett-Packard 8722ES network analyzer through S_{11} port measurements, as the probe moves above the tissue sample surface. The microwave excitation frequency of the resonant probe can be varied within the bandwidth of the network analyzer and is tuned to critical coupling by external capacitors. The *X*–*Y* axis stage is driven with Coherent® optical encoded dc linear actuators. The probe is frame mounted to a *Z*-axis linear actuator assembly and the height at which the probe is above the sample can be precisely set. The *X*–*Y* stage actuators, network analyzer, data acquisition and collection are controlled by the computer. The program that interfaces to the *X*–*Y* stage actuators, serial port

communications, 8722ES GPIB interface, and data acquisition is written in National Instruments Labview® software. The complete evanescent microwave scanning system is mounted on a vibration-dampening table.

4.3 Complex Permittivity Values of Porcine Skin Tissue from 1GHz to 15 GHz

The porcine skin tissue samples were acquired from a local slaughter facility and the time duration from death to tissue sample characterization was less than 2 hours. The tissue samples were refrigerated at approximately 40° F during transport. The origin of the porcine tissue samples used in this investigation are 18 to 20 month old males of american yorkshire type and shoulder location. A total of six random measurements using the two point method were made at each frequency with the tissue sample surface dry at a temperature of 289 K.

4.3.1 Results

Biological tissues are inhomogeneous and exhibit considerable variability in structural composition and, therefore dielectric properties. The ranges of complex dielectric measurements at each frequency along with the population mean (solid curve) are indicated in figures 4.2, 4.3 for the dielectric constant and dielectric loss respectively. The mean value of the data spread at each frequency is indicated by the solid blue curve and the actual data is denoted by solid red points.

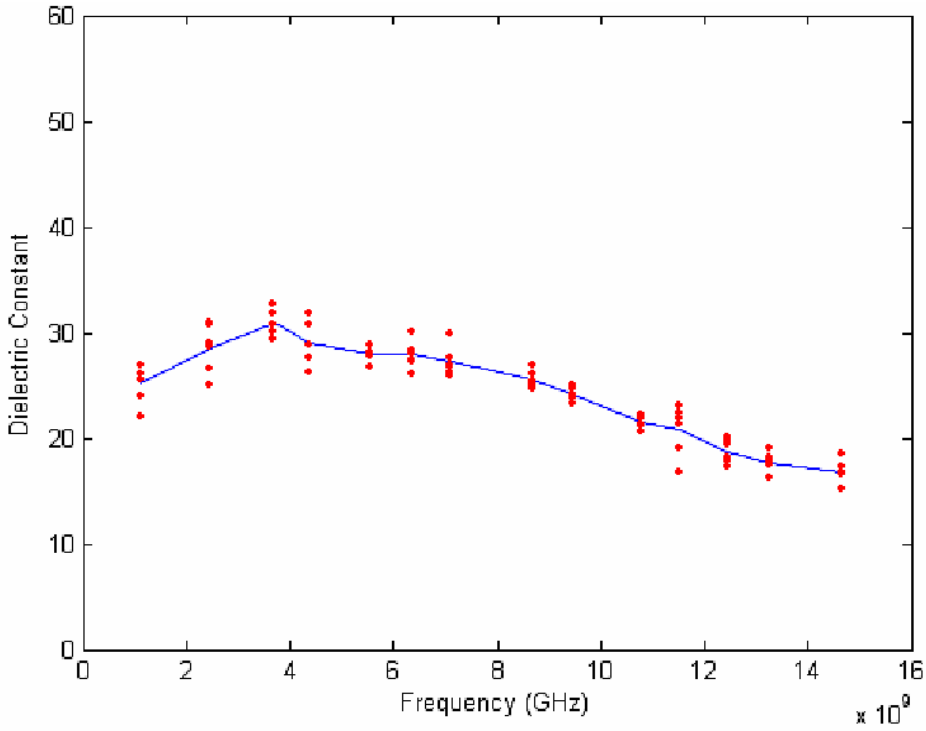

Fig. 4.2. Dielectric constant of porcine skin tissue from 1 GHz to 15 GHz.

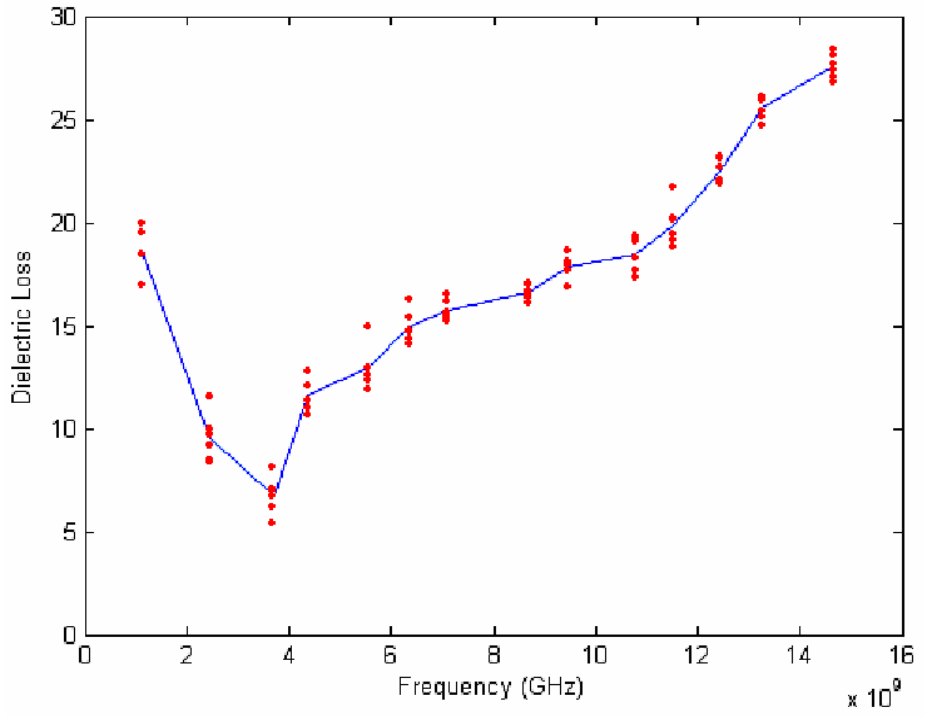

Fig. 4.3. Dielectric loss of porcine skin tissue from 1 GHz to 15 GHz.

The statistical data is based on six random readings at each frequency and given in Tables 4.1 and 4.2. The dielectric constant measurement results of our investigation ranged in values from 16.5 to 38.8. The dielectric loss values ranged from 5.4 to 28.5. The dielectric constant data measured in this study shows an increase from 1 to 3 GHz. and continues to reduce with increase in frequency according to γ dispersion, resulting from the polarization of water molecules [2].

TABLE 4.1. Dielectric constant mean and standard deviation vs. frequency.

Frequency GHz	Mean	Std. Dev.
1.116	25.25	1.943
2.451	28.483	2.368
3.699	30.916	1.205
4.363	29.08	2.239
5.544	28.066	0.742
6.364	27.9	1.331
7.088	27.216	1.499
8.665	25.583	0.837
9.473	24.116	0.649
10.776	21.533	0.634
11.537	20.75	2.361
12.445	18.716	1.1354
13.246	17.7	0.883
14.865	16.783	1.11

TABLE 4.2. Dielectric loss mean and standard deviation vs. frequency.

Frequency GHz	Mean	Std. Dev.
1.116	18.667	1.402
2.451	9.549	1.146
3.699	6.75	0.909
4.363	11.6	0.851
5.544	12.933	1.081
6.364	14.933	0.806
7.088	15.733	0.516
8.665	16.633	0.377
9.473	17.867	0.56
10.776	18.483	0.849
11.537	19.9	1.031
12.445	22.483	0.594
13.246	25.533	0.56
14.865	27.583	0.604

4.3.2 Conclusion

The dielectric constant data is similar to [3] although the trend of this data decreases from 1 to 2 GHz. and has a slight increase at approximately 3 GHz. The range of dielectric values for our data is 29 to 33 at 3 GHz compared to 38 to 40 for the data represented in [3]. The subjects used in our study were around 18 to 20 months old and the lower dielectric values in general may be associated to surface lipid chemical composition changes in the skin from birth to adolescence [4]. To compare measurement reproducibility between our study and a previous study, we calculated the standard error of the mean for the measurements in Tables 4.I and 4.II and obtained ranges of 0.025 to 0.966% for the dielectric constant, and 0.154 to 0.467% for dielectric loss. This level of variability is considerably smaller than the values of 5-10% for dielectric constant and 0.2 to 3% for dielectric loss [3]. This indicates that the evanescent probe design and technique described here might be more reproducible.

4.4 Tissue Puncture Lesion Scan and Measurement

A skin surface puncture lesion shown in figure 4.4 was characterized in a two step procedure. Initially the lesion was scanned with the resonant probe, producing a relative change in frequency, Q, and reflection coefficient images over the scan area. The image scan area is 3 mm x 3 mm with a probe standoff distance height of 10 μm above the tissue surface, an image resolution of 100 μm measurement steps, at a resonant frequency of 1.1373 GHz. Subsequently, complex dielectric measurements were performed using the methodology of section 3.2.2, 3.2.3, and Eqs. (3.48, 3.49) at points of interest in the relative change in Q image. Three dielectric measurements were taken approximately 500 μm from the center of the lesion about 120° apart and indicated at points (*A, B, C*). The second set of three

measurements were taken approximately 150 µm from the center of the lesion at roughly the same angular spacing at points (*D, E, F*), and the final measurement point is centered in the puncture lesion at point (*G).* It was noted that prior to characterization, the puncture lesion appeared to be an older wound. The puncture site had dark coagulated blood and the immediate adjacent tissue was raised and pink in color.

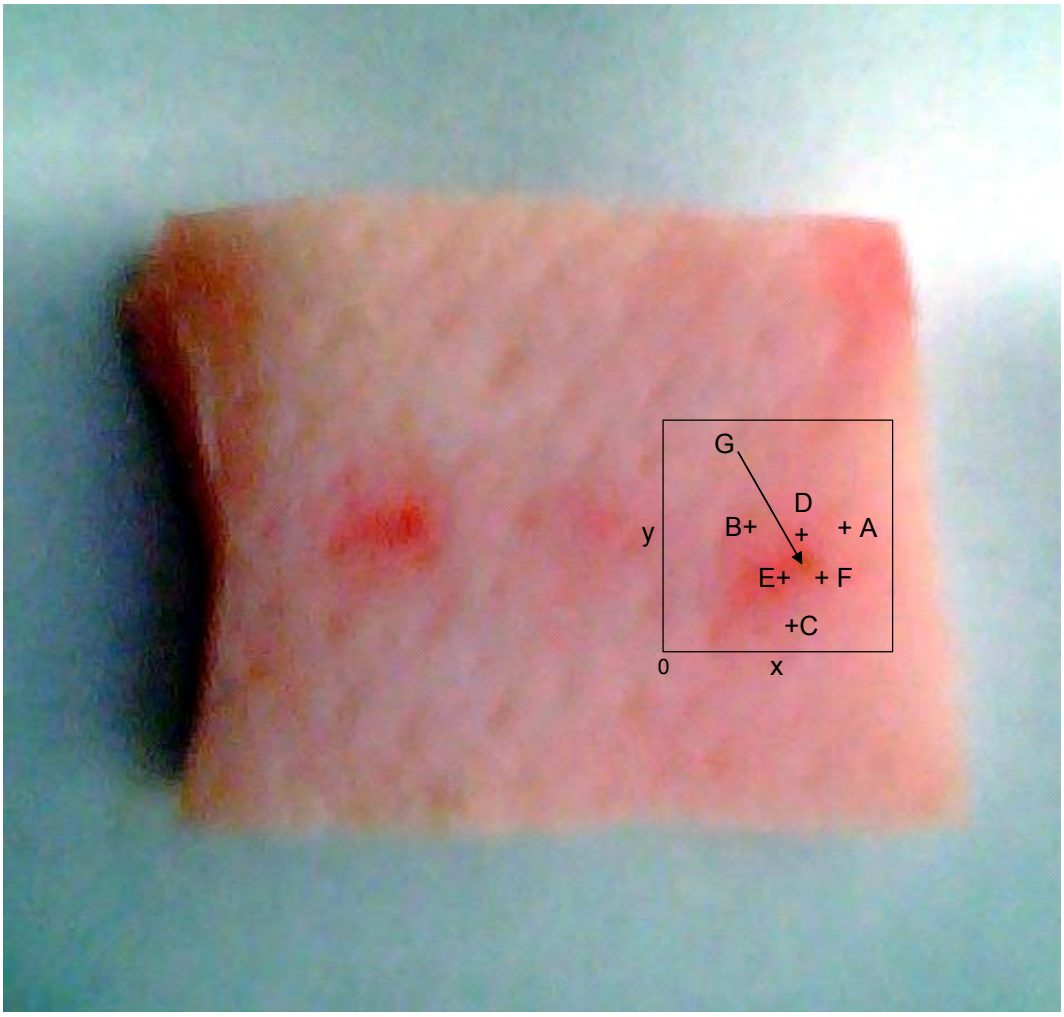

Fig. 4.4. Scan area of porcine skin puncture lesion.

4.4.1 Results

The surface puncture lesion of figure 4.4 was scanned, producing a change in frequency, Q, and reflection coefficient images illustrated in figures 4.5-4.7 respectively. The change in frequency image contains surface topography and dielectric properties, while the change in Q image shows variations in conductivity, which is the inverse of the change in reflection coefficient image and indicates resistive properties of the tissue sample. The total shift in resonant frequency and Q measurements were model fit, resulting in dielectric property values on and around the puncture lesion for seven separate locations. The real and imaginary parts of the complex dielectric measurement are given in Table 4.3.

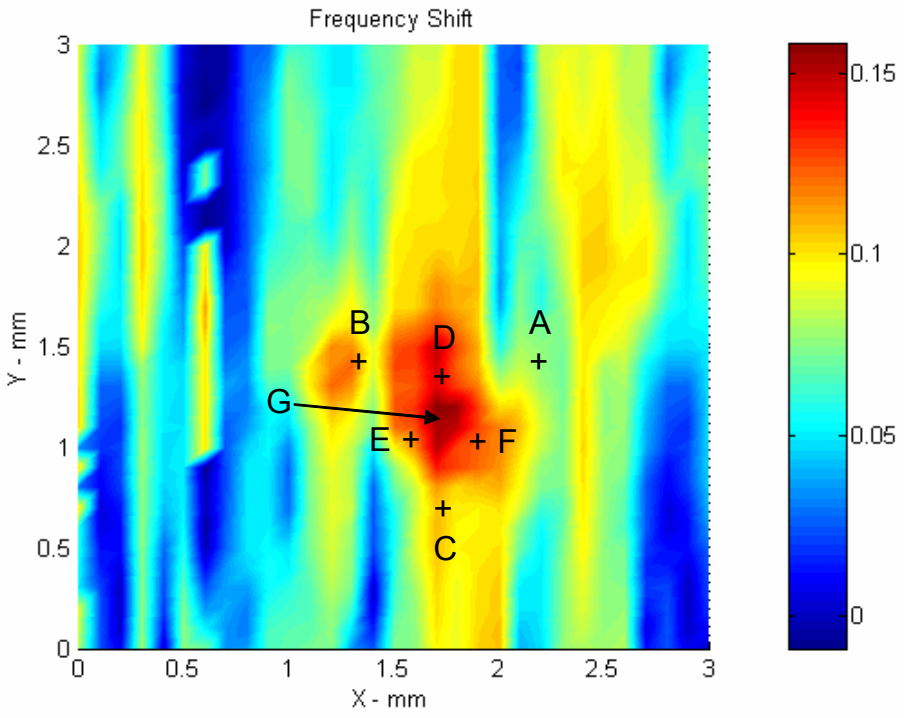

Fig. 4.5. Change in frequency image of tissue puncture lesion.

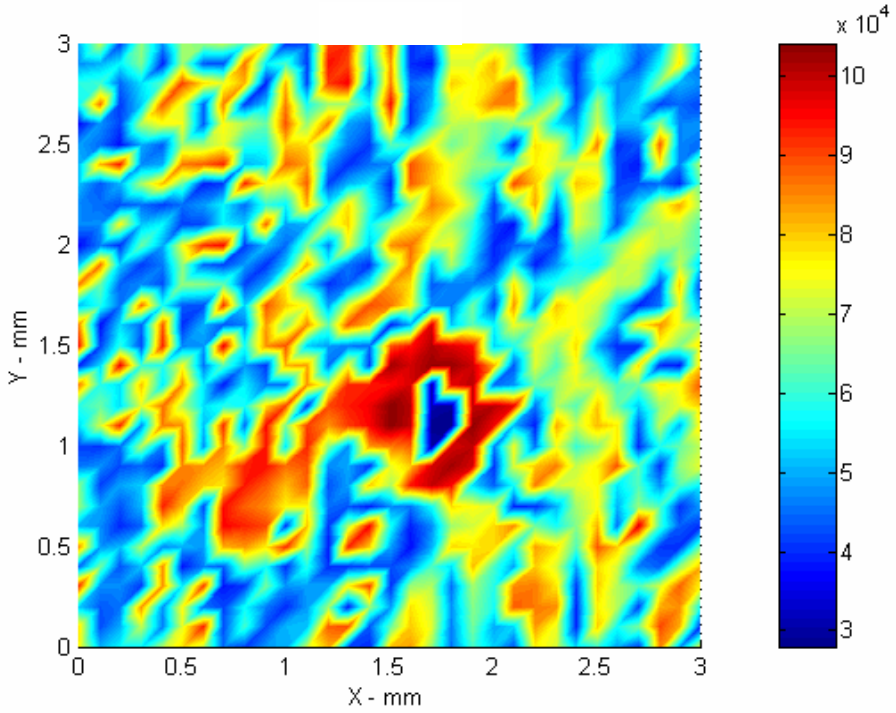

Fig. 4.6. Change in Q image of tissue puncture lesion.

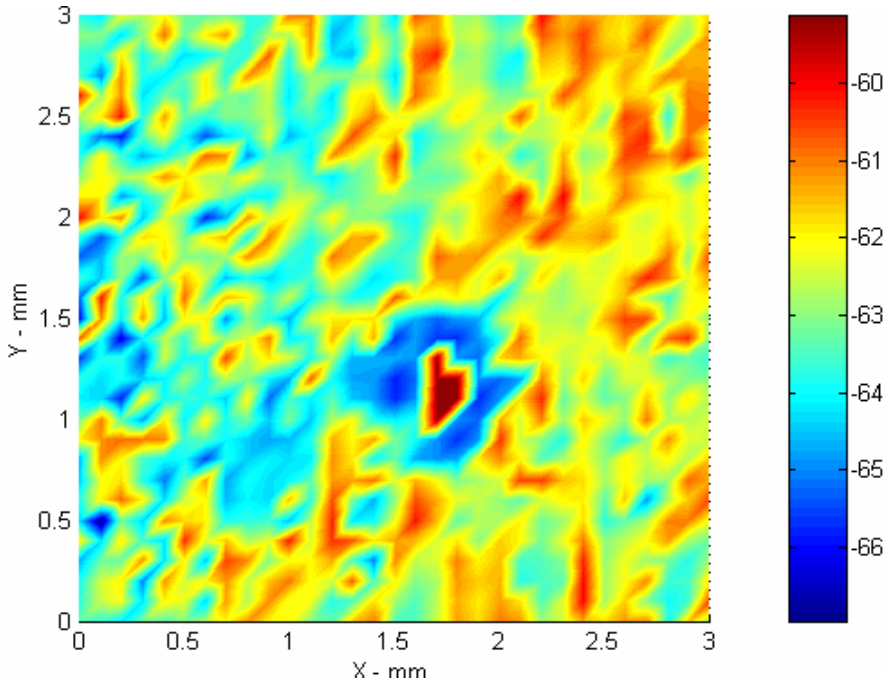

Fig. 4.7. Change in S_{11} image of tissue puncture lesion.

TABLE 4. 3. Tissue puncture lesion measurements and location.

Sample Point	Dielectric constant	Dielectric loss	Lesion center dist. (μm)
A	26.1	20	500
B	19	21.7	500
C	27	18.7	500
D	17.9	23.7	150
E	17.5	24.1	150
F	18.2	23.4	150
G	38	2.1	0

4.4.2 Conclusion

The outer most points (*A*-*C*) are comparable to normal tissue values. The immediate surrounding data (*D*-*F*) indicate a higher conductivity and lower dielectric constant, than measured at this frequency in normal tissues (figures 4.2 and 4.3 Tables 4.1 and 4.2). The measurement of the puncture lesion indicate a low conductivity and high dielectric constant at point (*G*), which is centered on the puncture wound and corresponds to dry coagulated blood cells. The age of the puncture wound and the possibility of dilated and leaking capillary beds and/or infection could explain the higher conductivity readings in the immediate surrounding tissue.

4.5 Complex Permittivity Measurements of Heat Damaged Tissue

Figure 4.8 shows five separate burn areas on the surface of an excised section of porcine tissue, where the burn areas are of increasing severity labeled 1-5. The subsurface tissue damage should vary according to depth of involvement, resulting from acute thermal contact. The five burn marks were induced by direct contact of a tip from a standard soldering instrument. A 600 °F iron was held under constant pressure on the tissue surface from 1 to 5 seconds in duration. A series of complex dielectric measurements were made by

moving the probe at several separate locations within each burn location area at a frequency of 1.1373 GHz.

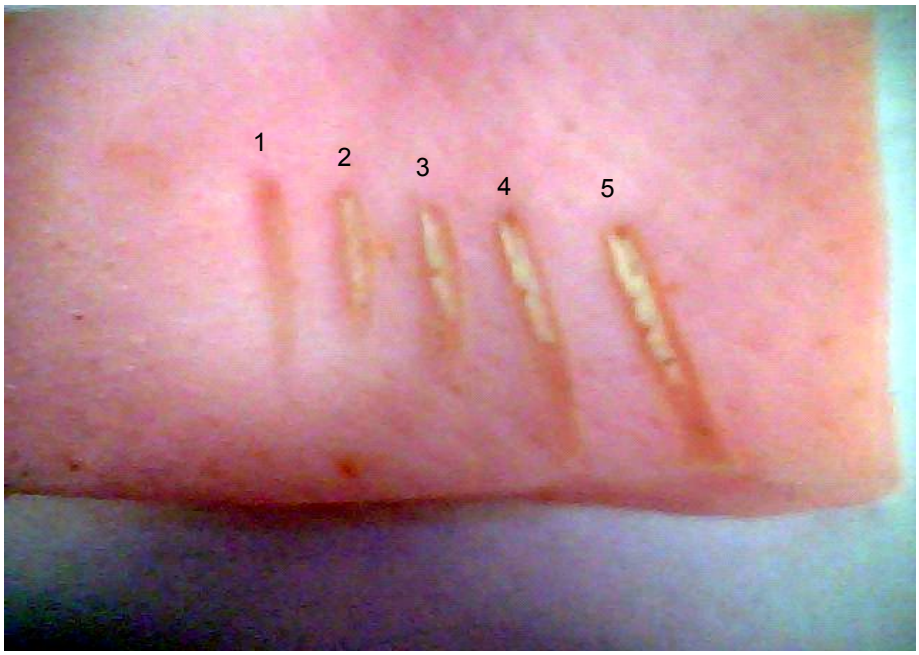

Fig. 4.8. Skin surface burns (1) 600 °F 1sec., (2) 600 °F 2sec., (3) 600 °F 3sec., (4) 600 °F 4sec., and (5) 600 °F 5sec.,

4.5.1 Results

The tissue surface burn data shown in Table 4.4 for section (1) shows a higher dielectric constant and slightly lower related loss in comparison to the normal tissue values. This result could be an effect of reducing moisture in the outermost epidermal layer. Section (2) data shows an increase in conductivity and decrease in dielectric constant from the data for section (1). A possible explanation is a further thermal disruption of the skin, releasing water, ions, and plasma proteins from the interstitial fluid due to tissue denaturing and micro vascular damage [5]. The data of section (3) shows a significant decrease in conductivity, which may be due to additional fluid evaporation and thickness damage. The burn data of

sections (4, 5) indicate a continued decrease in dielectric constant and loss from interstitial fluid evaporation and thermal degradation of the tissue.

TABLE 4. 4. Tissue burn lesion section measurement mean.

Section	Dielectric constant (mean)	Dielecric loss (mean)
1	45.22	16.6
2	32.98	19.98
3	37.8	3.25
4	21.38	2.82
5	8.68	0.304

4.5.2 Conclusion

The burn data indicates appreciable dielectric property differences with thermal damage levels and shows promise that the evanescent technique could be used for burn evaluation. Although, the research was conducted *in vitro* and live tissue exhibits full physiological and anatomical functional activity when burned, an *in vivo* study may still produce significant enough thermal level data differences to make the technique useful.

4.6 Evanescent Field Depth and Subsurface Structure Detection in Skin Tissue

A series of two line scan measurements were performed with the evanescent probe across the surface of an excised section of porcine tissue, resulting in two single line maps of the change in quality factor profile of the non-uniformities, depth-wise in the tissue sample. The scan parameters for the tissue sample are resonant frequency f_0 = 1.1373 GHz with a probe tip standoff distance of 5 μm above the tissue surface and 10 μm step intervals recording a resonant quality factor profile over a scan length of 2000 μm. The resonant f_0 was chosen because it is the $\gamma/4$ fundamental frequency of the probe. Following the scans, the porcine skin was fixed in 10% formalin in phosphate-buffered saline, dehydrated in ethanol, and embedded in paraffin. Sections approximately 10 μm in thickness and 2000 μm in length

were mounted on glass slides and stained in hematoxylin and eosin and photographed for comparison against the line scan change in Q signature, which corresponds to the variance in conductivity.

4.6.1 Results

Figures 4.9, 4.10 illustrate the ΔQ line scan signal from the probe and corresponding sub-surface tissue histological structure. The prepared tissue slides and line scan measurements show a relation of ΔQ (conductivity) signal strengths and corresponding biological structures such as ducts of exocrine sweat glands, and vein lumen ducts. The tissue slide sample edges were curled during processing and the tissue appears to be slightly stretched, but the tissue structure-signal match up can be seen fairly well. The longest skin structure seen by the probe is the exocrine duct in figure 4.9 between 0.6 mm and 1.0 mm on the X axis and extends from the surface to approximately 0.375 mm into the dermis. There is a large signal peak between 0.5 mm to 0.1 mm that could be due to a gland or vein that is out of the plane of the slide since the histology slice is only 10 μm, whereas the spatial region being detected by the probe certainly includes an area wider than 10 μm. In figure 4.10 there are three vein ducts, two of which are distinct, traversing the dermis tissue in the plane of the slide and are shown at 0.0-0.25 mm, 0.5-0.8 mm and 1.0-1.3 mm on the X axis. There is also a signal peak between 1.4 mm and 1.9 mm that does not correspond to any sub surface feature in the histology slide, which again may be due to a structure outside of the plane of the slide. The depths of the vein lumen are approximately from 0.25 mm to 0.3 mm. The majority of the smaller signal peaks may correspond to capillary beds near the surface, which reveal residual blood serum from the staining process and are considered more conductive

than dielectric and/or spatial heterogeneity. The capillary beds are located under the epidermis layer and have an average depth of 35 microns.

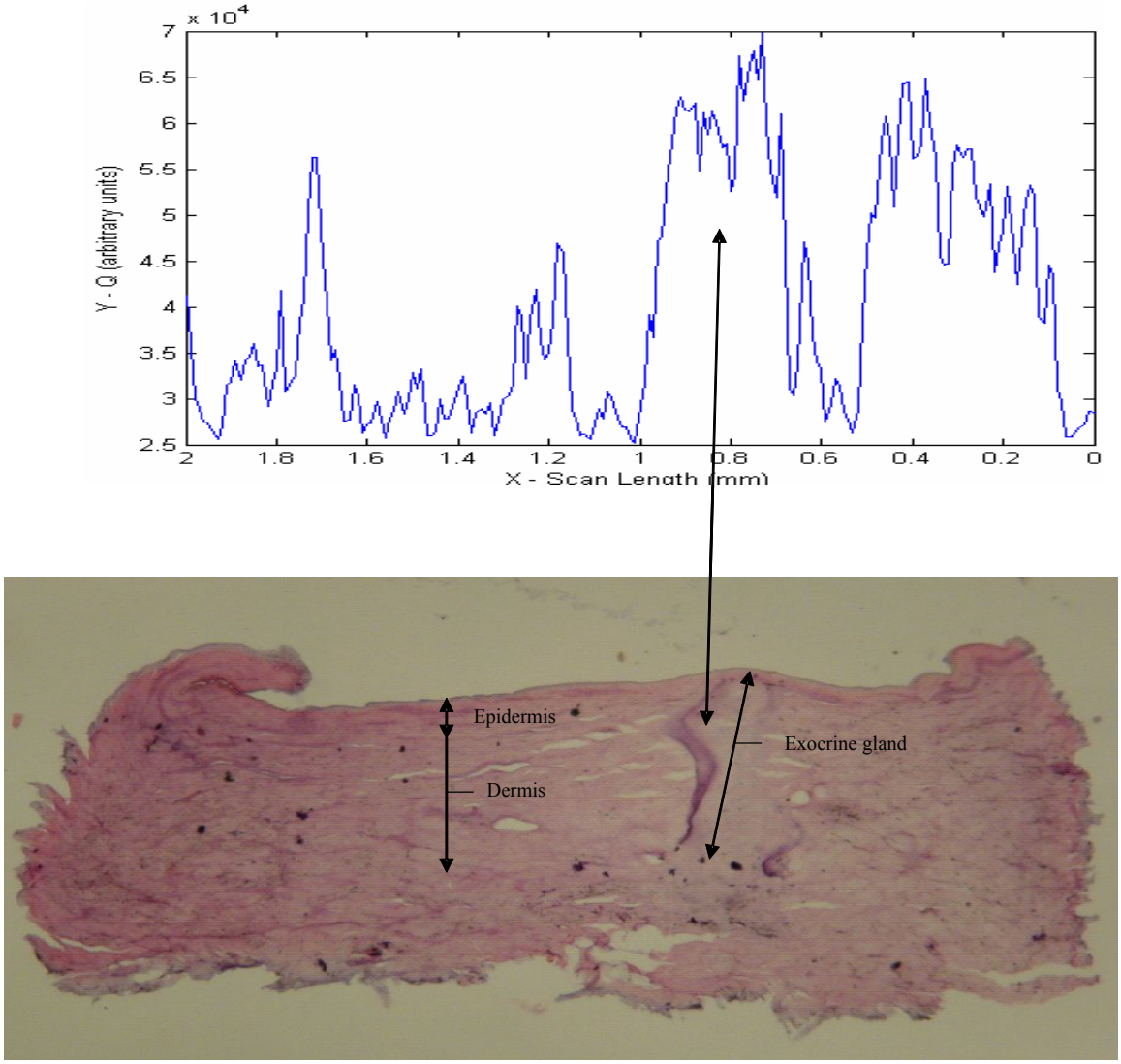

Fig. 4.9. ΔQ line-scan of tissue showing correspondence of signal peaks with capillary beds and exocrine gland.

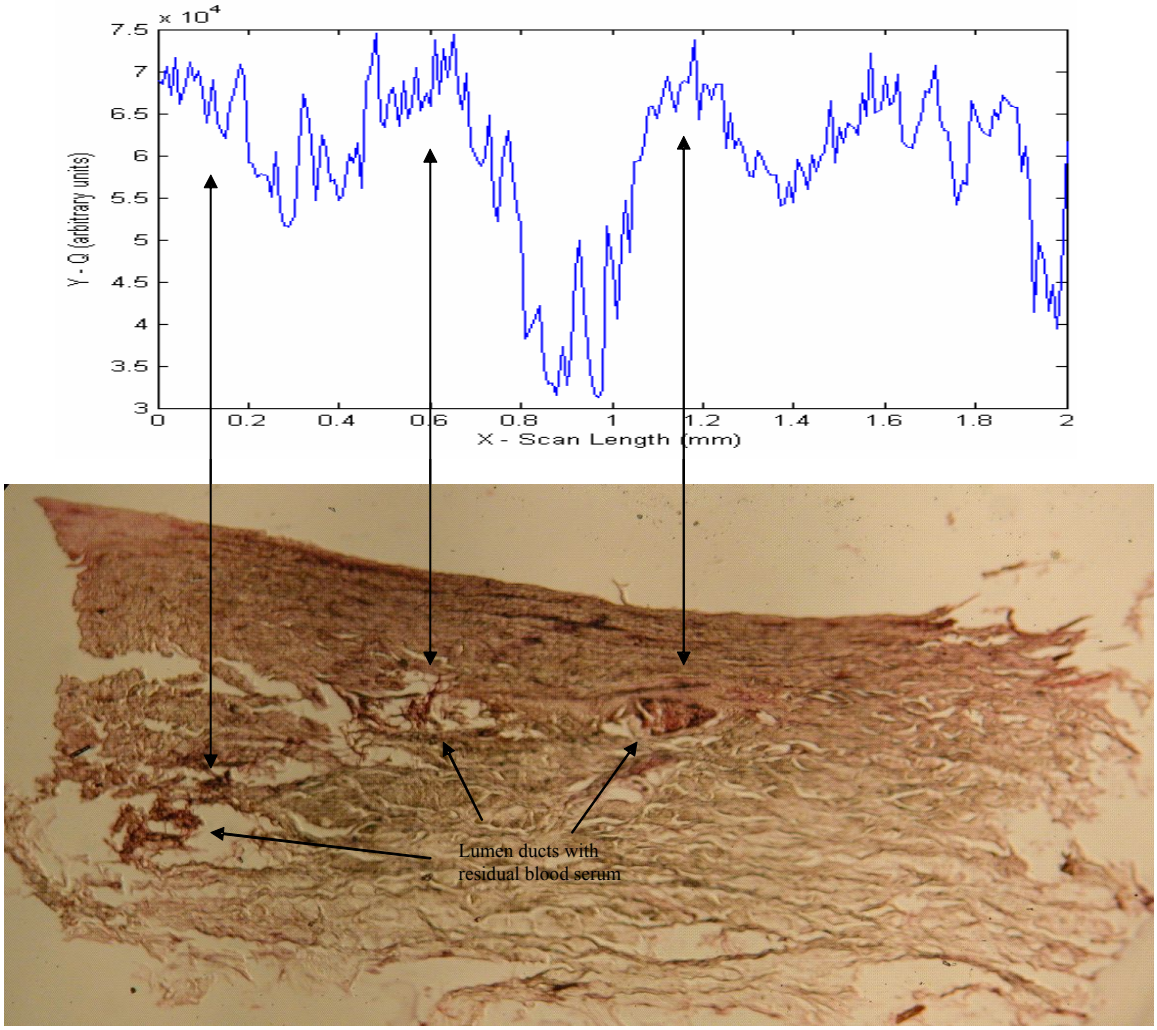

Fig. 4.10. ΔQ line-scan of tissue showing correspondence of signal peaks with the lumen of a vein moving in and out of the plane of section.

4.6.2 Conclusion

The probe tip radius is 10 μm and the spatial resolution of the probe is governed by this physical dimension, but the aperture diameter along with the tissue properties dictates the evanescent field decay length. The corresponding ΔQ signal widths will be slightly larger than the lumen ducts and gland structures the evanescent field detects at tissue depths within the decay length of the field, due to the three dimensional penumbral effect of the field

emanating off the probe tip and widening depth-wise. This sensor appears that it could be used for superficial wound and burn assessment, but as far as the applicability to deep lacerations the device is presently limited from deep field penetration depth.

4.7 Chapter 4 References

[1] R.A. Kleismit, G. Kozlowski, R.R. Biggers, I. Maartense, M.K. Kazimierczuk and D.B. Mast, "Characterization of local dielectric properties of superconductor $YBa_2Cu_3O_{7-\delta}$ using evanescent microwave microscopy," IEEE Trans.Appl.Supercond., vol.15, pp.2915-2918, 2005.

[2] M. A. Stuchly and S. S. Stuchly, Electrical properties of biological substances, Biological Effects and Medical Applications of Electromagnetic Energy, ed. O. P. Gandhi, Printice Hall, New Jersey ,1990.

[3] K.O. Olawale, R.J. Petrell, D.G. Michelson, and A.W. Trites, "The dielectric properties of the cranial skin of five young captive stellar sea lions and a similar number of young domestic pigs and sheep between 0.1 and 10 GHz," Physiol Meas. vol. 26, pp.627-637, 2005.

[4] P. Ramasastry, D. T. Downing, P. E. Pichi, and J. S. Srauss,"Chemical composition of human skin surface lipids from birth to puberty," J. Invest. Dermatol,, vol. 54, pp. 139-144, 1970.

[5] L. Devgan, B. Satyanarayn, S. Aylward, and R. Spence, "modalities for the assessment of burn wound depth,"Journal of Burns and Wounds," vol. 5, pp. 7-15, 2006.

5 Conclusion

5.1 Summary

The motivation of this research is to develop a new two point measurement theory based on the method of images to investigate the complex permittivity of biological materials independent of their electrical properties, through evanescent microwave microscopy. This type of characterization is accomplished by tracking total perturbational changes in the resonant frequency and quality factor (Q) of a coaxial transmission line resonator with a tungsten tip protruding through an end-wall aperture. A quantitative relationship between the real and imaginary parts of the local dielectric constant of porcine skin tissue and the total resonant frequency and Q shift using the method of images was established. The resonant frequency and Q shift versus probe tip-sample separation curve is linearly fit to generate these parameters. The comparison between experimental and literature data based on this method is shown for porcine skin tissue at room temperature (298 K).

The sensor is used to measure the complex permittivity frequency response from 1 GHz to 15 GHz of excised porcine skin tissue. A superficial tissue puncture lesion was scanned producing a change in frequency, quality factor, and reflection coefficient images of the lesion and surrounding area along with complex permittivity measurements. A quantitative analysis of varying, tissue surface, heat damage was presented as well as a quality factor surface scan signal profile that correlates the signal with subsurface tissue structures. The dielectric properties of the porcine skin tissue within the near field of the tip frustrate the electric field and measurably changes the transmission line's resonant frequency and quality

factor. In the quantitative analysis the total shift of the resonator's frequency and quality factor is measured as a function of tip-sample separation and associated changes in quality factor image scans of the biological tissue are presented. A comparison between experimental data produced in this study and existing in literature from 1 to 15 GHz as well as theory based on the two and multi-point quantitative methods is given and discussed for freshly excised porcine skin tissue and conform well to theoretical predictions.

The design and fabrication of a resonant coaxial type probe that is simply evanescent in the near-field is presented and discussed. The spatial resolution of the probe is experimentally verified and an analysis of probe sensitivity through first order estimations generated from equivalent circuit models for the probe, conductor, and dielectric, is shown.

5.2 Implications

This experimental exercise produced dielectric constant and loss measurements that were carried out *in vitro* on freshly excised tissue. The technique used in this study produced dielectric and conductivity values and trends for porcine skin tissue consistent with those seen by the open-ended coaxial technique. The results indicate that this technique could be used for superficial wound assessment, but as far as the applicability to deep wounds the device is presently limited by penetration depth. The burn data indicates appreciable dielectric property differences with thermal damage levels and shows promise that the evanescent technique could be used for burn evaluation. Although, the research was conducted *in vitro* and live tissue exhibits full physiological and anatomical functional activity when burned, an *in vivo* study may still produce significant enough thermal level data differences to make the technique useful. Basal cell carcinoma, squamous cell

carcinoma, malignant melanoma and Kaposi's sarcoma are dependent upon new blood vessel growth for their development and progression. The cutaneous melanomas and carcinomas usually originate in the epidermal compartment and in the vertical growth phase will require a blood supply to sustain growth. The sensor discussed here shows a potential in monitoring skin tumor angiogenesis and performance of endogenous inhibitors, although more research is required to determine if the sensor is capable to detect and differentiate skin melanoma and carcinoma.

5.3 Major Contributions

The major contributions of this body of knowledge are summarized as follows.

- Complete derivation of the electrostatic field outside the probe tip and within the sample for two point perturbational quantitative method
- Development of a quantitative relationship between the real and imaginary parts of the local dielectric constant the resonant frequency and Q shift of the resonant probe using the method of images, resulting in a methodology applicable to biological samples
- Experimental verification of evanescent microwave measurement system and two point model for biological applications.
- Proof of concept as tool for the non-destructive evaluation of superficial skin lesions.
- First order estimation of probe / measurement system sensitivity.
- Experimental verification of probe spatial resolution.

5.4 Future Work

The evanescent microwave microscopy system described here has numerous areas to explore. The first of which could be modifications to the existing model to allow measurement of a multilayer system. The capability of producing complex permittivity values of single layer dielectrics can be extended to a two layer system for measurement of thin films. This would require a known base dielectric with an unknown thin film dielectric coating. This would also require the dielectric parameters b of Equation (3.38) to be two separate complex dielectrics, where the number of model fit variables will remain the same due to the base dielectric being a known value. This would also require the reformulation of the model frequency shift solution equation as a result of added boundary conditions and modified field perturbations from the second dielectric.

The sensor and methodology show a potential in monitoring skin tumor angiogenesis and performance of endogenous inhibitors, although more research is required to determine if the sensor is capable to detect and differentiate skin melanoma and carcinoma. The evanescent technique indicates promise for burn evaluation, although there is more investigation needed to demonstrate the sensor is capable of determining tissue heat damage *in vivo*.

The two point model consists of frequency and Q shift solutions for the total perturbed electric field outside the tip and in the sample. An enhancement to the current model would be the addition of the frequency shift component due to the perturbed magnetic field outside the tip and above the sample.